Journal of Non-Newtonian Fluid Mechanics 327 (2024) 105221

Contents lists available at ScienceDirect

Journal of Non-Newtonian Fluid Mechanics

journal homepage: www.elsevier.com/locate/jnnfm

Full length article

Impact of drops of a nanoparticle dispersion in a viscoelastic liquid

Takshak Shende *, Ian Eames, Mohammad Hadi Esteki, Yousef Javanmardi, Emad Moeendarbary *

Department of Mechanical Engineering, University College London, Torrington Place, London WC1E 7JE, United Kingdom

ARTICLE INFO

Keywords:
Viscoelastic fluid
Nanoparticle dispersion
Shear-thinning fluid
Droplet impact
Eulerian–Lagrangian
Volume of fluid
OpenFOAM
Wettability

ABSTRACT

The evaluation of nanoparticle dispersion within viscoelastic fluids upon impact on hydrophobic and hydrophilic surfaces is conducted using the Euler-Lagrangian technique. The volume-of-fluid approach is employed in conjunction with the Lagrangian method to model the transport of nanoparticles in a three-phase system (particles-air-viscoelastic fluid). The assessment of nanoparticle dispersion was conducted over a range of Péclet numbers and contact angles (θ = 30° and 120°) in three-dimensional (3D) space using the mean square displacement method. The findings suggest that the dispersion of nanoparticles is mainly influenced by normal stress. During droplet impact, nanoparticles exhibit non-Fickian superdiffusive behaviour due to the viscoelastic fluid's non-Gaussian distribution of velocity and stresses (normal and shear) fields. The wettability of the fluid with solid surfaces substantially affected the dispersion of nanoparticles in the viscoelastic fluid.

1. Introduction

Bio-aerosol transport, biofluid transport, drug delivery, spray coatings, inkjet printing, and the impact of raindrops on leaves are just a few examples of the many natural and industrial processes that rely on the interaction of droplets with solid surfaces. Numerous surgical procedures conducted within hospital settings result in the generation of bioaerosols derived from biofluids [1,2]. Biofluids are known to include viruses and bacteria at the nano- and microscales. Most of these biological fluids exhibit viscoelastic characteristics [3–6]. Viruses and bacteria can be regarded as nanoparticles to assess their dispersion within biofluids when subjected to the impact of biofluids on a solid surface.

Due to the complex interaction of nonlinear material rheology, fluid inertia, elasticity, and fluid–structure interactions, developing robust and accurate simulation methods for the simulation of viscoelastic fluid flow dynamics is difficult [7–9]. The presence of particles in the fluids affects the transmission of stress during fluid–particle interaction and the interaction between particles and solid surfaces at the boundary [10]. Biological fluids and non-Newtonian polymeric fluids may exhibit shear-thinning, shear-thickening, or viscoelastic properties, respectively, in response to the solvent-incorporated material's chemical and physical properties [5,8,11]. Introducing particulate matter within the non-Newtonian fluid introduces additional complexities in the interplay of momentum exchange between the fluid and particles at the microscopic level [12]. As a result, accurately forecasting the continuum scale response of this multiphase system becomes an immense challenge both experimentally and computationally [10,13].

Modelling nanoparticle mobility in fluids requires the use of computational approaches. To evaluate the dynamics of particle-laden viscoelastic fluids, numerical techniques, including the lattice Boltzmann method [14–16], finite difference method [17,18], finite element method [19], finite volume method [9,10], and smoothed particle hydrodynamics [20], were applied. Using the discrete element method (DEM) in conjunction with computational fluid dynamics (CFD) facilitates a deeper understanding of the intricate dynamics governing particle–fluid and particle–particle interactions [10,12,21]. However, due to the paucity of information regarding the number of particles, precise rheological properties of the fluid, and flow characteristics, it is difficult to obtain fast and accurate predictions of particle-laden viscoelastic fluid flow. Numerous constitutive equations are available in the literature to model viscoelastic fluids, such as Oldroyd-B, Giesekus, and Phan-Thien-Tanner (PTT) models [22]. Each viscoelastic model has its limitations [11]. For example, it has been discovered that when the fluid's deformation rate is significantly greater than the relaxation time of the microstructure, the Oldroyd-B model performs inadequately [11]. The Phan-Thien–Tanner model [23] is developed based on the network theory for polymeric solutions, while the Oldroyd-B [24] and Giesekus [25] models are developed based on the concept of an elastic spring attached to two beads in a polymeric solution.

Recent studies, Ayar et al. [12], Fernandes et al. [10], and Faroughi et al. [9,26] evaluated the drag force acting on spherical particles moving through viscoelastic fluids modelled with the Oldroyd-B and

* Corresponding authors.
E-mail addresses: t.shende@ucl.ac.uk (T. Shende), i.eames@ucl.ac.uk (I. Eames), e.moeendarbary@ucl.ac.uk (E. Moeendarbary).

https://doi.org/10.1016/j.jnnfm.2024.105221
Received 21 September 2023; Received in revised form 15 March 2024; Accepted 19 March 2024
Available online 22 March 2024

Giesekus constitutive equations by developing and employing a CFD-DEM method. Zhang and Shaqfeh [13,27] utilised the finite volume method, as proposed by Yang et al. [28], to investigate the impact of polymer concentration and volume fraction of a non-colloidal rigid sphere in viscoelastic fluids modelled with Oldroyd-B and Giesekus constitutive equations on shear rheology. These investigations demonstrate that the microscale and continuum-scale dynamics of particles in viscoelastic fluids are affected by the first normal stress difference that the fluid experiences. This suggests that particle dispersion in a viscoelastic fluid is thus significantly impacted by the normal stress field within the fluid.

The complexity of analysing particle-laden viscoelastic fluid flow increases when particles in the fluid interact with a two-phase system that has a fluid–fluid interface. Depending on the properties of the two fluids and a solid surface, the fluid–fluid interface deforms under the influence of forces within a viscoelastic fluid (*e.g.* viscous, elastic, *etc.*) and outside fluid (*e.g.* fluid–fluid interfacial tension) and its interaction forces with a solid boundary (*e.g.* contact angle). Complex interactions in three-phase systems involving particles and fluids can be simulated by combining the Euler-Lagrangian [10,21] and Volume of Fluid (VoF) [29] approaches. The Lagrangian tracking technique improves the computational framework by exposing particle-level behaviour and interactions [30]. This methodology makes monitoring nanoparticles, analysing their trajectories, and anticipating their dispersion patterns easier. In this paper, we developed a three-phase volume-of-fluid-Lagrangian method for viscoelastic fluids to simulate the droplet impact of particle-laden viscoelastic fluids on a solid surface.

Droplet impact of Newtonian and non-Newtonian fluids on hydrophilic and hydrophobic surfaces has been extensively studied from a spatial and temporal perspective [31–35]. The wettability of the surface governs droplet impact on the surface. The dynamics of droplets as they spread out and recede from a surface and eventually separate from it have been studied in great detail [31,36–38]. Incorporating nanoparticles into a viscoelastic fluid results in distinct spreading and splashing mechanisms compared to the Newtonian solvent. This is due to the influence of the viscoelastic fluid's elongation properties on the interactions between the particles and the fluid and the interface between air and liquid [36]. The wettability of interfaces between fluids and solids has a significant influence on the dispersion of nanoparticles. The interactions between nanoparticles and the substrate upon impact are influenced by how much a fluid wets a surface [32,39]. The wetting behaviours of hydrophobic and hydrophilic surfaces differ, leading to variations in the contact area, adhesion, and consequent dispersion of nanoparticles [32]. Research has demonstrated the critical importance of surface wettability in controlling the fate of nanoparticles and, thus, dispersion of nanoparticles in various fluidic settings, demonstrating its relevance across numerous applications [31,32,40–44]

The processes of advection and diffusion regulate the dispersion of nanoparticles. The advection process occurs when a fluid's bulk motion carries a particle while preserving its properties. Diffusion, conversely, is the net movement of particles due to particle random motion from a higher concentration to a lower concentration without the bulk flow of a fluid. Thus, the Péclet number, a parameter that quantifies the relative significance of advection and diffusion, is a crucial factor in determining the dispersion characteristics of nanoparticles [21,45,46]. Previous research has investigated the impacts of varying Péclet numbers on the dispersion and migration of nanoparticles, providing insights into the intricate relationship between advection and diffusion mechanisms [46,47]. Furthermore, the investigation of the contact angle, which serves as an indicator of the fluid's wetting characteristics on solid surfaces, has been thoroughly examined in several contexts [31,32,40–43]. The investigation of the influence of contact angle on nanoparticle dispersion yields significant insights into the interfacial phenomena that dictate the interactions between particles and surfaces [44].

The majority of research conducted on the phenomenon of dispersion has mostly concentrated on fluids that adhere to Newtonian principles [48–54]. There is a limited body of work that has examined the dispersion of nanoparticles by monitoring their movement within viscoelastic fluids [47,55–59]. While there has been considerable research conducted on particle tracking in Newtonian fluids and two-dimensional porous media [30,48,60], there is currently a lack of comprehensive investigations regarding the dispersion of nanoparticles inside viscoelastic fluids in a three-dimensional (3D) context. The influence of dimensionality on hydrodynamic interaction varies between two-dimensional (2D) and three-dimensional (3D) systems [46,61]. Prior investigations of nanoparticle tracking have predominantly been conducted within a limited spatial domain in two dimensions, primarily due to constraints imposed by available instrumentation.

Viscoelastic fluids exhibit viscoelastic instability while flowing through contraction and curved channels due to the fluid's elastic properties and extra polymer stress [8,62]. This viscoelastic instability significantly affects solute and nanoparticle dispersion in the viscoelastic fluid [47,62]. The investigation of the dynamics of the dispersion of nanoparticles inside viscoelastic fluids resulting from the impact of droplets holds significant importance in many industrial applications [63]. It has been found that viscoelastic rheological properties play a crucial role in determining how fluid particles move [63]. Although the impact of the particle-laden viscoelastic droplet on surfaces has been studied experimentally [36,63,64], numerical simulation of the particle-laden viscoelastic droplet is scarce, and thus, it is not clear whether normal stress or elastic instability contribute to the enhancement or suppression of the dispersion of particles during droplet impact.

The impact of droplets of particle-laden viscoelastic fluid on both hydrophobic and hydrophilic solid surfaces was investigated in this work. We chose the PTT viscoelastic model, as we have shown in our earlier work [29] that the PTT model can be adapted to upscale the rheological properties of the non-Newtonian fluid from the pore scale to Darcy's scale in a porous medium [29]. The discrepancy between droplet dynamics and particle dispersion, as simulated by the PTT and Oldroyd-B models, is examined. We demonstrated that increasing particle concentration enhances the droplet's initial momentum, resulting in distinct spatial and temporal stress patterns and particle dispersion. The primary objective of this study is to provide two novel contributions. To the best of our knowledge, there has been no prior investigation on incorporating nanoparticles as a distinct phase inside a three-phase (particles-fluid-air) simulation study utilising the volume-of-fluid-Lagrangian approach for viscoelastic fluids. Specifically, this study focuses on the influence of a viscoelastic fluid droplet on hydrophilic and hydrophobic surfaces in a three-dimensional context. Furthermore, our findings demonstrate anomalous characteristics of nanoparticle dispersion when viscoelastic fluid droplets collide over a range of Péclet numbers. It has been demonstrated that the spatial variation in normal stress influences the dispersion of nanoparticles.

2. Governing equations

The volume-of-fluid-Lagrangian approach is employed to examine the migration of nanoparticles suspended within a viscoelastic fluid during droplet impact. The governing equations of the viscoelastic Phan-Thien–Tanner fluid are solved using RheoTool [65] implemented in the OpenFOAM C++ library [66]. The movements of the nanoparticles are projected by utilising the flow field that has been previously computed and applying Newton's second law at every incremental time interval.

2.1. Eulerian frame: Volume-of-fluid method

The equation of motion of viscoelastic fluids with velocity field $\boldsymbol{u}_\mathrm{f}$ and time t is defined using continuity equation ($\boldsymbol{\nabla}\cdot\boldsymbol{u}_\mathrm{f}=0$) and momentum equation [11],

$$\rho_\mathrm{f}\left(\frac{\partial \boldsymbol{u}_\mathrm{f}}{\partial t}+\boldsymbol{u}_\mathrm{f}\cdot\boldsymbol{\nabla}\boldsymbol{u}_\mathrm{f}\right)=\boldsymbol{\nabla}\cdot\boldsymbol{\sigma}+\mathbf{F}_{\boldsymbol{\gamma}}-\mathbf{S}_\mathrm{p}, \tag{1}$$

where ρ_f is the fluid density, $\boldsymbol{\sigma}$ is the total fluid stress tensor, $\mathbf{F}_\gamma$ is the interfacial force, and $\mathbf{S}_p$ represents an extra source term that accounts for the influence of particle forces on the fluid flow during each iteration. The stress tensor $\boldsymbol{\sigma}$ in Eq. (1) can be decomposed into three components: a pressure term ($-p\mathbf{I}$), the Newtonian part represented by $\boldsymbol{\tau} = 2\mu\mathbf{D}$, and the viscoelastic part denoted as $\boldsymbol{\sigma}_p$,

$$\boldsymbol{\sigma} = -p\mathbf{I} + \boldsymbol{\tau} + \boldsymbol{\sigma}_p, \tag{2}$$

where p is the pressure, μ is the solvent viscosity, $\mathbf{I}$ is the identity tensor, $\boldsymbol{\sigma}_p$ is the polymeric stress tensor, and $\mathbf{D} = \frac{1}{2}\left(\nabla\boldsymbol{u}_f + (\nabla\boldsymbol{u}_f)^T\right)$ is the rate of deformation tensor.

The constitutive equation for polymeric stress tensor $\boldsymbol{\sigma}_p$ contribution, based on network theory for polymeric solutions, is defined by the Phan-Thien–Tanner model [23,67,68] as follows:

$$f(\boldsymbol{\sigma}_p)\boldsymbol{\sigma}_p + \lambda\overset{\square}{\boldsymbol{\sigma}}_p = 2\eta_p\mathbf{D}, \tag{3}$$

where $\overset{\square}{\boldsymbol{\sigma}}_p$, is the Gordon–Schowalter derivative of $\boldsymbol{\sigma}_p$,

$$\overset{\square}{\boldsymbol{\sigma}}_p = \overset{\nabla}{\boldsymbol{\sigma}}_p + \zeta(\boldsymbol{\sigma}_p\cdot\mathbf{D} + \mathbf{D}\cdot\boldsymbol{\sigma}_p), \tag{4}$$

$$\overset{\nabla}{\boldsymbol{\sigma}}_p = \frac{\partial\boldsymbol{\sigma}_p}{\partial t} + \boldsymbol{u}_f\cdot\nabla\boldsymbol{\sigma}_p - \boldsymbol{\sigma}_p\cdot\nabla\boldsymbol{u}_f - (\nabla\boldsymbol{u}_f)^T\cdot\boldsymbol{\sigma}_p, \tag{5}$$

where $\overset{\nabla}{\boldsymbol{\sigma}}_p$ is the Oldroyd's upper-convected derivative of $\boldsymbol{\sigma}_p$ [24], λ is the characteristic relaxation time, and η_p is the polymeric fluid contribution to the zero shear viscosity (η_0) *i.e.* $\eta_0 = \eta_p + \mu$. The PTT model's parameter ζ accounts for the slip between the polymer's molecular network and the continuous fluid medium. The $\zeta = 0$ represents affine, and $\zeta \neq 0$ represents a non-affine version of the rheological model. While numerous viscoelastic polymeric fluids exhibit polymeric slip at the microscale, we encountered difficulties in accurately determining the proper value of ζ based on experimental data available in the literature. Thus, we have employed the affine version (with $\zeta = 0$) of the PTT model. As a result, the upper-convected derivative was utilised in Eq. (3). Phan-Thien and Tanner originally defined the stress invariant function $f(\boldsymbol{\sigma}_p)$ in Eq. (3) using the linear form as $f(\boldsymbol{\sigma}_p) = 1 + \frac{\varepsilon\lambda}{\eta_p}\mathrm{tr}(\boldsymbol{\sigma}_p)$ [23,69], where ε represents the viscoelastic fluid's extensional properties, which is inversely proportional to the fluid's extensional viscosity [68]. Phan-Thien later suggested an exponential equation, $f(\boldsymbol{\sigma}_p) = e^{\frac{\varepsilon\lambda}{\eta_p}\mathrm{tr}(\boldsymbol{\sigma}_p)}$, in 1978, which considers the exponential increase in strain under intense flow [67]. It should be noted that if $f(\boldsymbol{\sigma}_p) = 1$ and $\zeta = 0$, then Eq. (3) becomes the Oldroyd-B equation [24]. For weak flow (e.g. viscometric flow), the PTT model predicts the dynamics viscosity η of the fluid as [67],

$$\eta = \frac{\eta_0}{1 + \varepsilon(2-\varepsilon)\lambda^2\dot{\gamma}^2}. \tag{6}$$

The polymer within the polymeric fluid undergoes various levels of stretching, entanglement, and compression. The conformation tensor $\mathbf{A}$ describes the extent to which a polymer is stretched in a fluid [22,70]. The polymer stress vanished when $\mathbf{A} = \mathbf{I}$ in the limit of a long time [22]. The $\boldsymbol{\sigma}_p$ of the PTT model as function of $\mathbf{A}$ is given by,

$$\boldsymbol{\sigma}_p = \frac{\eta_p}{\lambda}\left[\mathbf{A} - \mathbf{I}\right]. \tag{7}$$

The evolution of $\mathbf{A}$ using the linear form of PTT is [22],

$$\overset{\nabla}{\mathbf{A}} = \frac{1 + \varepsilon\,(\mathrm{tr}\mathbf{A} - 3)}{\lambda}[\mathbf{A} - \mathbf{I}], \tag{8}$$

and evolution of $\mathbf{A}$ using exponential form of PTT is,

$$\overset{\nabla}{\mathbf{A}} = \frac{e^{\varepsilon(\mathrm{tr}\mathbf{A}-3)}}{\lambda}[\mathbf{A} - \mathbf{I}], \tag{9}$$

where $\overset{\nabla}{\mathbf{A}}$ is the upper-convected derivative of $\mathbf{A}$,

$$\overset{\nabla}{\mathbf{A}} = \frac{\partial\mathbf{A}}{\partial t} + \boldsymbol{u}_f\cdot\nabla\mathbf{A} - \mathbf{A}\cdot\nabla\boldsymbol{u}_f - (\nabla\boldsymbol{u}_f)^T\cdot\mathbf{A}. \tag{10}$$

The flow of viscoelastic polymeric fluids, represented by $\boldsymbol{u}_f$ for advection and $\nabla\boldsymbol{u}_f$ for stretching and re-orientation of the polymer, are depicted in Eq. (10). The restoring elastic term is proportional to $\mathbf{A}$ [70].

The conformation tensor is a second-order tensor that is both symmetric and positive-definite. Therefore, it can be expressed as the factorisation of $\mathbf{R}\boldsymbol{\Lambda}\mathbf{R}^\mathbf{T}$, where $\mathbf{R}$ represents the matrix of eigenvectors of $\mathbf{A}$ and $\boldsymbol{\Lambda}$ represents the diagonal matrix of eigenvalues obtained from $\mathbf{A}$. Guenette et al. (1995) proposed the inclusion of a diffusion term $\boldsymbol{\nabla}\cdot(\eta_p\boldsymbol{\nabla}\boldsymbol{u}_f)$ on both sides of the momentum Eq. (1) in order to enhance the stability of numerical simulations [71,72]. Both terms cancel each other out once a steady state is achieved. Thus, Eq. (1) becomes [73,74],

$$\rho_f\left(\frac{\partial\boldsymbol{u}_f}{\partial t} + \boldsymbol{u}_f\cdot\boldsymbol{\nabla}\boldsymbol{u}_f\right) - \boldsymbol{\nabla}\cdot\left[(\mu+\eta_p)\boldsymbol{\nabla}\boldsymbol{u}_f\right] = -p\mathbf{I} - \boldsymbol{\nabla}\cdot\left(\eta_p\boldsymbol{\nabla}\boldsymbol{u}_f\right) + \boldsymbol{\nabla}\cdot\boldsymbol{\sigma}_p + \mathbf{F}_\gamma - \mathbf{S}_p. \tag{11}$$

The stress experienced during the impact of a viscoelastic droplet on a solid surface exhibits an exponential increase, particularly at the interface between the solid and liquid when the droplet's contact line advances and recedes. The rapid increase in the magnitude of stress may result in numerical instability issues while conducting simulations. Thus, we have employed the log-conformation tensor method, accessible in RheoTool [65,73], to mitigate numerical stability issues [75,76]. In this particular methodology, the constitutive equation is redefined by employing the logarithm of the conformation tensor, denoted as $\boldsymbol{\Theta} = \ln(\mathbf{A}) = \mathbf{R}\boldsymbol{\Lambda}^{\boldsymbol{\Theta}}\mathbf{R}^T$ and $\boldsymbol{\Lambda} = \exp(\boldsymbol{\Lambda}^{\boldsymbol{\Theta}})$. This reformulation allows the stress field to be linearised in regions with exponential growth while guaranteeing that the conformation tensor stays positive-definite [73]. As a result, this strategy improves numerical stability [73,76]. Eq. (7) of linear PTT model is solved in term of $\boldsymbol{\Theta}$ as,

$$\frac{\partial\boldsymbol{\Theta}}{\partial t} + \boldsymbol{u}_f\cdot\nabla\Theta - (\boldsymbol{\Omega}\boldsymbol{\Theta} - \boldsymbol{\Theta}\boldsymbol{\Omega}) - 2\mathbf{B} = \frac{f}{\lambda}(e^{-\boldsymbol{\Theta}} - \mathbf{I}), \tag{12}$$

where $f = 1 + \varepsilon[\mathrm{tr}(e^{\boldsymbol{\Theta}}) - 3]$ for the linear PTT, $f = e^{\varepsilon[\mathrm{tr}(e^{\boldsymbol{\Theta}})-3]}$ for the exponential PTT, and

$$\mathbf{M} = \mathbf{R}\boldsymbol{\nabla}\boldsymbol{u}_f^T\mathbf{R}^T = \begin{bmatrix} m_{xx} & m_{xy} & m_{xz} \\ m_{yx} & m_{yy} & m_{yz} \\ m_{zx} & m_{zy} & m_{zz} \end{bmatrix}, \tag{13}$$

$$\boldsymbol{\Omega} = \mathbf{R}\begin{bmatrix} 0 & \omega_{xy} & \omega_{xz} \\ -\omega_{xy} & 0 & \omega_{yz} \\ -\omega_{xz} & -\omega_{yz} & 0 \end{bmatrix}\mathbf{R}^T, \tag{14}$$

$$\mathbf{B} = \mathbf{R}\begin{bmatrix} m_{xx} & 0 & 0 \\ 0 & m_{yy} & 0 \\ 0 & 0 & m_{zz} \end{bmatrix}\mathbf{R}^T, \tag{15}$$

where $\omega_{ij} = \frac{\Lambda_j m_{ij} + \Lambda_i m_{ji}}{\Lambda_j - \Lambda_i}$. Finally, the polymeric stress is computed using $\boldsymbol{\sigma}_p = \frac{\eta_p}{\lambda}[e^{\boldsymbol{\Theta}} - \mathbf{I}]$. Readers are referred to [65,73,75–78] for more details.

In the volume-of-fluid method for two-phase flows, the above equations are solved simultaneously with the transport equation for phase volume fraction α ($0 \le \alpha \le 1$),

$$\frac{\partial\alpha}{\partial t} + \boldsymbol{\nabla}\cdot(\alpha\boldsymbol{u}_f) + \boldsymbol{\nabla}\cdot(\alpha(1-\alpha)\boldsymbol{u}_{f,r}) = 0, \tag{16}$$

where $\boldsymbol{u}_{f,r} = \boldsymbol{u}_1 - \boldsymbol{u}_2$ is the relative velocity between two phases. The artificial interface compression term, $\boldsymbol{\nabla}\cdot(\alpha(1-\alpha)\boldsymbol{u}_{f,r})$, guarantees the sharpness of the interface [79–82]. For sharpness and boundedness, the term $\alpha(1-\alpha)$ ensures that compression is active in the interfacial region where $0 < \alpha < 1$ [79,82]. The numerical diffusion is controlled by discretisation of relative velocity (for more details, please refer to [81,82]). At fluid–fluid interface, $\rho = \alpha\rho_1 + (1-\alpha)\rho_2$ and $\eta = \alpha\eta_1 + (1-\alpha)\eta_2$. ρ_i and η_i represents density and viscosity of i fluid, respectively. The interfacial force in Eq. (1) [83] is

$$\mathbf{F}_\gamma = \gamma\,\kappa(\boldsymbol{\nabla}\alpha), \tag{17}$$

where γ is the interfacial tension, and $\kappa = -\boldsymbol{\nabla} \cdot \frac{\boldsymbol{\nabla}\alpha}{|\boldsymbol{\nabla}\alpha|}$ is the interfacial curvature. The equilibrium contact angle θ at fluid–solid interface satisfies $\hat{\boldsymbol{n}} \cdot \boldsymbol{n}_s = \cos\theta$, where $\boldsymbol{n}_s$ and $\hat{\boldsymbol{n}}$ are the unit vector normal to the wall and fluid–fluid interface respectively.

2.2. Lagrangian frame

The motion of individual nanoparticles with mass m_p and velocity $\boldsymbol{v}_\mathrm{p}$ in the Lagrangian framework is governed by Newton's second law Eq. (18) [21,59,84,85],

$$m_\mathrm{p} \frac{\mathrm{d}\boldsymbol{v}_\mathrm{p}}{\mathrm{d}t} = \mathbf{F}_\mathrm{C} + \mathbf{F}_\mathrm{F}, \tag{18}$$

where $\mathbf{F}_\mathrm{C}$ is the contact forces acting on the particles due to interparticle interaction or particle–wall interactions and $\mathbf{F}_\mathrm{F}$ is the particle–fluid interaction forces acting on particles. As the particles move through the fluid, they experience different forces due to the interaction between the particles and the fluid [21,46,59,86–89]. However, we defined particle–fluid forces as [21,46],

$$\mathbf{F}_\mathrm{F} = \mathbf{F}_\mathrm{G,B} + \mathbf{F}_\mathrm{B} + \mathbf{F}_\mathrm{D}, \tag{19}$$

where $\mathbf{F}_\mathrm{G,B}, \mathbf{F}_\mathrm{B}, \mathbf{F}_\mathrm{D}$ are the combined gravity and buoyancy force, the Brownian motion force, and the drag force, respectively. The $\mathbf{F}_\mathrm{G,B}$ due to gravity g is determined using [21,59,87],

$$\mathbf{F}_\mathrm{G,B} = m_\mathrm{p}\, g \left(1 - \frac{\rho_\mathrm{f}}{\rho_\mathrm{p}}\right), \tag{20}$$

where ρ_p is the density of the particle. Nanoparticles exhibit Brownian motion, which is a stochastic movement caused by their interactions with nearby molecules, owing to their small size [46,61]. This motion is anticipated to significantly influence the dispersion of these nanoparticles within a fluid medium under the influence of flow [21,89]. The nanoparticle experiences a stochastic Brownian force ($\mathbf{F}_\mathrm{B}$) due to thermal fluctuations in the fluid, which is defined as a Gaussian white noise random process [90],

$$\mathbf{F}_\mathrm{B} = \xi_\mathrm{i} \left(\frac{\pi}{\Delta t} \delta_\mathrm{ij} \frac{216\, \nu\, k_\mathrm{B}\, T}{\pi^2\, d_\mathrm{p}^5\, \rho_\mathrm{f}\, C_\mathrm{c} \left(\frac{\rho_\mathrm{p}}{\rho_\mathrm{f}}\right)^2} \right)^{\frac{1}{2}}, \tag{21}$$

where k_B is the Boltzmann constant, Δt is the time step, ξ_i is the Gaussian random number with zero mean and unit variance, d_p is the diameter of the particle, T is the temperature, δ_ij is the Kronecker delta function, ν is the kinematic viscosity. The Stokes–Cunningham slip correction, $C_\mathrm{c} = 1 + \frac{2\lambda_\mathrm{m}}{d_\mathrm{p}} \left(1.257 + 0.4e^{\frac{1.1 d_\mathrm{p}}{2\lambda_\mathrm{m}}}\right)$, is a function of the molecular mean free path (λ_m) [89]. It should be noted that the temperature of the fluid influences the fluid's viscosity and density along with Brownian movements of the nanoparticles [91]. As a result, the flow was assumed to be isothermal with a constant temperature of 300 K. The drag force ($\mathbf{F_D}$) acting on the particle is given by

$$\mathbf{F_D} = \frac{3\, C_\mathrm{d}\, Re_\mathrm{p}\, m_\mathrm{p}\, \eta\, \left(\boldsymbol{u}_\mathrm{f} - \boldsymbol{v}_\mathrm{p}\right)}{4\, \rho_\mathrm{p}\, d_\mathrm{p}^2}, \tag{22}$$

where C_d is the drag coefficient, and $Re_\mathrm{p} = \frac{\rho u_0 d_\mathrm{p}}{\eta_0}$ is the particle Reynolds number. In this work, we selected $C_\mathrm{d} Re_\mathrm{p} = 24(1 + \frac{1}{6} Re_\mathrm{p}^{2/3})$ since the Re_p is less than 100 [59].

A simplified model comprising of a Hertzian spring-slider-dashpot system [59,86,92], implemented in the OpenFOAM, is utilised to calculate the contact forces resulting from particle collisions. The dashpot is a representation of viscous dissipation, while the spring is a representation of elastic deformation. The Hertzian contact theory [86,92] establishes that the stiffness coefficient for the collision between two spherical particles of equal size is $k_\mathrm{n} = \frac{\sqrt{d_p} E_\mathrm{p}}{3(1-\chi_\mathrm{p})}$ in the normal direction and $k_\mathrm{t} = \frac{2\sqrt{d_\mathrm{p}} G_\mathrm{p}}{3(2-\chi_\mathrm{p})} \delta_\mathrm{n}$ in the tangential direction, where E_p, χ_p, G_p and δ_n are the particle's Young's modulus, Poisson ratio, shear modulus and normal direction displacement, respectively. Similarly, the stiffness coefficient for the collision between particle i and wall w is denoted as $k_\mathrm{nw} = \frac{\sqrt{8 d_\mathrm{p}/3}}{\frac{1-\chi_\mathrm{p}^2}{E_\mathrm{p}} + \frac{1-\chi_\mathrm{w}^2}{E_\mathrm{w}}}$ in the normal direction and $k_\mathrm{tw} = \frac{2\sqrt{4 d_\mathrm{p}} G_\mathrm{p}}{2-\chi_\mathrm{p}} \delta_\mathrm{n}$ in the tangential direction [86,92], where E_w, χ_w, and δ_tw are the wall's Young's modulus, Poisson ratio, and tangential direction displacement, respectively. The damping coefficient in both the normal and tangential directions is obtained using $\psi_\mathrm{n} = Y(m_\mathrm{p} k_n)^{1/2} \delta_\mathrm{n}^{1/4}$, where Y is an empirical constant which is a function of the coefficient of restitution (e) [92]. The total force $\mathbf{F}_\mathrm{C}$ exerted on particle i by its neighbouring particle j (or by wall w) as a result of particle–particle collision $\mathbf{F}_\mathrm{p,ij}$ and particle–wall collision $\mathbf{F}_\mathrm{w,i}$ will be

$$\mathbf{F}_\mathrm{C} = \mathbf{F}_\mathrm{p,ij} + \mathbf{F}_\mathrm{w,i}, \tag{23}$$

$$\mathbf{F}_\mathrm{p,ij} = \sum_\mathrm{j} \left[\left(-k_\mathrm{n} \delta_\mathrm{n}^{1.5} - \psi_\mathrm{n} \boldsymbol{U}_\mathrm{nij} \cdot \boldsymbol{n}_\mathrm{p}\right) \boldsymbol{n}_\mathrm{p}\right] + \left[-k_\mathrm{t} \delta_\mathrm{t} - \psi_\mathrm{t} \boldsymbol{U}_\mathrm{sij}\right], \tag{24}$$

$$\mathbf{F}_\mathrm{w,i} = \sum_\mathrm{w} \left[\left(-k_\mathrm{nw} \delta_\mathrm{nw}^{1.5} - \psi_\mathrm{nw} \boldsymbol{U}_\mathrm{niw} \cdot \boldsymbol{n}_\mathrm{w}\right) \boldsymbol{n}_\mathrm{w}\right] + \left[-k_\mathrm{tw} \delta_\mathrm{tw} - \psi_\mathrm{tw} \boldsymbol{U}_\mathrm{siw}\right], \tag{25}$$

where δ_t and ψ_t are the displacement and damping coefficient in the tangential direction during particle–particle interaction; δ_nw and ψ_nw are the displacement and damping coefficient in the normal direction during particle–wall interaction; ψ_tw is the damping coefficient in the tangential direction during particle–wall interaction. $\boldsymbol{U}_\mathrm{nij}$ is the velocity vector of particle i relative to particle j; $\boldsymbol{U}_\mathrm{sij}$ is the slip velocity of the particle–particle contact point, $\boldsymbol{U}_\mathrm{niw}$ is the velocity vector of particle i relative to the wall w; $\boldsymbol{U}_\mathrm{siw}$ is the slip velocity of the particle contact point with the wall. The unit vector $\boldsymbol{n}_\mathrm{p}$ points from particle i's centre to particle j's centre, and the unit vector $\boldsymbol{n}_\mathrm{w}$ points from particle i's centre towards the wall. For a comprehensive explanation of particle contact forces, readers are directed to the work of [21,59,85,86,92].

Fernandes et al. [10] integrated the Lagrangian library [59] of OpenFOAM with the RheoTool [65,73] to conduct simulations of viscoelastic flow with particles, a two-phase system involving viscoelastic fluid and particles [10]. In the present study, we have integrated the Lagrangian library of OpenFOAM with the volume-of-fluid method employed in the RheoTool. This enabled us to conduct simulations involving particles in a two-phase system consisting of air and a viscoelastic fluid. Consequently, our system can be considered a three-phase system, encompassing particles, air, and the viscoelastic fluid. The *rheoInterFoam* solver of RheoTool [65] was modified to perform a three-phase numerical simulation.

We utilised the MULES (Multidimensional Universal Limiter with Explicit Solution) limiter, which guarantees boundedness by constraining the value of α to the range between 0 and 1, regardless of the particular numerical scheme and mesh structure utilised [81,93]. The Laplacian term was discretised utilising the Gauss linear corrected scheme, whereas the gradient and divergence terms of the governing equations were discretised employing the Gauss linear scheme. To compute the convective term in the governing equation, the Convergent and Universally Bounded Interpolation Scheme for the Treatment of Advection (CUBISTA) was utilised [7,73] which enhances the numerical stability. The time derivative was discretised using the Euler scheme. The pressure field was solved utilising a geometric agglomerated algebraic multigrid (GAMG) solver with diagonal incomplete-Cholesky (DIC) smoother, whereas the estimation of the stress field and velocity field was conducted with a preconditioned (bi-) conjugate gradient (PBiCG) solver with diagonal incomplete-lower–upper (DILU) preconditioning. The SIMPLEC (Semi-Implicit Method for Pressure-Linked Equations-Consistent) algorithm was implemented for pressure–velocity coupling. An absolute tolerance of 10^{-10} was established for pressure, velocity, and stress fields. The Euler scheme was employed to integrate velocity in the context of Lagrangian particle transport.

2.3. Numerical domain and boundary conditions

We simulated the impact of particle-laden viscoelastic fluids on a solid surface in three dimensions (3D). Boundary conditions of no-slip for velocity, fixed flux pressure for pressure, and constant contact angle for phase volume fraction were used on the solid surface (bottom). In the computational domain, pressure was subjected to a fixed value boundary condition at the top and sides, while velocity and phase volume fraction were subjected to a zero gradient boundary condition. At the start of the simulation, the whole computational domain around the droplet was filled with air. There were more than 15.8 million cells in the computational domain. We performed a grid convergence study at a droplet impact velocity of 0.4 m/s on a hydrophobic surface. After a grid density of 900 cells/mm^3, the simulation demonstrates a negligible variation in values of viscosity and velocity. Despite the high computational cost, all simulations were run with a grid density of more than 5000 cells/mm^3, Courant number, $Co = \boldsymbol{u}_f \Delta t/\Delta x$, of 0.05, and a time step Δt of 10^{-6} s to maintain convergence and accuracy, where Δx is the length interval. The computationally expensive simulations were conducted in parallel using University College London's high-performance computing cluster facility.

2.4. Dispersion coefficient (D)

The Stokes–Einstein equation was used to determine the molecular diffusion coefficient D_{SE} of spherical nanoparticles in a viscoelastic fluid [94],

$$D_{\mathrm{SE}} = \frac{k_{\mathrm{B}}T}{3\pi\eta_0 d_{\mathrm{p}}}. \tag{26}$$

We tracked the movement of the individual particles in the fluid. We fitted the linear portion of the mean square displacement (MSD) curve $\langle \mathbf{r}(t')^2 \rangle = 2\mathrm{D}\,t'$ to obtain the dispersion coefficient (D) [48,94]. The MSD of the nanoparticles was estimated using $\langle \mathbf{r}(t')^2 \rangle = \langle (\mathbf{r}(t+t') - \mathbf{r}(t'))^2 \rangle$, where t' is a lag time, $\mathbf{r}(t)$ is position of nanoparticles in fluid at time t, and $\langle\,\rangle$ is used to denote an ensemble value. The dispersion coefficient was normalised by D_{SE}. To evaluate the correlation of nanoparticle transport with Pèclet number Pe, the velocity autocorrelation function (VACF), $C_{\mathrm{L,T}}(t') = \langle \left(v_{\mathrm{x,y}}(t+t') - \langle v_{\mathrm{x,y}} \rangle\right)\left(v_{\mathrm{x,y}}(t) - \langle v_{\mathrm{x,y}} \rangle\right) \rangle$, was used, where $v_{\mathrm{x,y}}(t)$ is the velocity of a nanoparticle at the beginning of its trajectory, and $v_{\mathrm{x,y}}(t+t')$ is the velocity of nanoparticles after a lag time t', and $\langle v_{\mathrm{x,y}} \rangle$ represents the mean velocity of nanoparticles across all time and trajectories [21,95].

Péclet number $Pe = \frac{U_0 \delta_{\mathrm{L}}}{D_{\mathrm{SE}}}$ indicate the relative variation in the rate of advection and diffusion of nanoparticles, where, U_0 is the velocity of the viscoelastic droplet, and δ_{L} is the characteristic length scale (here initial diameter of the droplet $D_{d,0}$). The dimensionless time is defined as $t_D = \frac{t\,U_0}{\delta_L}$. Weber number $We = \frac{\rho_{\mathrm{f}} U_0^2 D_{d,0}}{\gamma}$ indicate the relative variation in the inertial and surface tension forces. Capillary number $Ca = \frac{\eta_p U_0}{\gamma}$, indicates the relative variation between viscous forces and surface tension forces. Weissenberg number $Wi = \frac{U_0 \lambda}{D_{d,0}}$ indicate the relative variation in elastic and viscous forces. The Deborah number $De = \frac{\lambda}{t_p}$ indicates how fluid behaves over a given time-frame, where t_p is a characteristic time of the deformation process. Ohnesorge number $Oh = \frac{\eta_{\mathrm{p}}}{\sqrt{\gamma \rho_{\mathrm{f}} D_{d,0}}}$ indicates the relationship between viscous, inertial and surface tension forces.

We performed three sets of numerical experiments. In the first set, we simulated the impact of a particle-laden polyethylene oxide (PEO) droplet (having 10^6 silica nanoparticles) of 2 mm diameter on a hydrophobic surface ($\theta = 160°$) and a dilute polyethylene oxide droplet (without particles) of 3 mm diameter on a hydrophobic surface ($\theta = 106°$) to validate the numerical method. In the second set, we simulated the impact of xanthan gum droplets (having 100 and 10000 soda lime microspheres) of 2 mm diameter on a hydrophobic surface ($\theta = 120°$) using the PTT and Oldroyd-B models and compared it with the impact of a particle-laden Newtonian fluid. In the third set of experiments, we simulated the impact of a particle-laden dilute PEO fluid droplet (having 5000 silica nanoparticles) of 1 mm diameter on a hydrophilic ($\theta = 30°$) and hydrophobic ($\theta = 120°$) surface over a range of Pe. Fig. 1 shows that experimentally observed viscometric data of PEO fluid of Zang et al. [64] and xanthan gum fluid of Campagnolo et al. [96] fits with equation (6) of PTT model using model parameters given in the description of Fig. 1. Validation of the PTT model for PEO fluid is given in section S1 of the supporting information (SI).

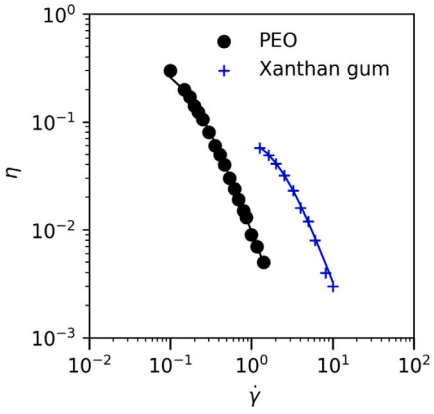

Fig. 1. Viscometric data of shear viscosity–shear rate of PEO fluid of Zang et al. [64], and xanthan gum fluid of Campagnolo et al. [96] fitted with Eq. (6) of PTT model using following model parameters. [Zang et al.: $\eta_{\mathrm{p}} = 0.35$ Pa s, $\lambda = 6$ s, and $\varepsilon = 0.85$; Campagnolo et al.: $\eta_{\mathrm{p}} = 0.08$ Pa s, $\lambda = 1.1$ s, and $\varepsilon = 0.1$. The solid line is PTT model prediction using Eq. (6).

3. Results and discussion

3.1. Validation

The three-phase numerical model was validated against experimental data from Zang et al. [64]. The droplet ($D_{\mathrm{d,0}} = 2$ mm) of polyethylene oxide (PEO) with silica nanoparticles ($d_{\mathrm{p}} = 0.2$ microns) impacting a hydrophobic surface ($\theta = 160°$) exhibits spatial and temporal variation as shown in Fig. 2b and simulation clip 1 attached in the supplemental information (SI) at an impact velocity of 0.88 m/s. The silica nanoparticle had a density ρ_{p} of 2000 kg/m^3, a Young modulus E_{p} of 7.1×10^{10} N/m^2, and a Poisson's ratio χ_{p} of 0.16 [97]. The 10^6 nanoparticles were randomly distributed in the viscoelastic fluids at the start of the simulation, accounting for approximately volume fraction ϕ of 10^{-5}. We assumed the temperature of the fluid as 300 K and the mean free path of the particle as 10^{-9} m. The rheological properties of the PEO fluid available in [64] were $\eta_{\mathrm{p}} = 0.35$ Pa s, $\eta_s = 0.005$ Pa s, and $\gamma = 0.0592$ N/m. We assumed that the density, relaxation time, and PTT extensibility parameters of the PEO fluid were $\rho_{\mathrm{f}} = 1000$ kg/m^3, $\lambda = 6$ s, and $\varepsilon = 0.85$, respectively, and the density and viscosity of the air were $\rho_{\mathrm{a}} = 1$ kg/m^3 and $\mu_{\mathrm{a}} = 10^{-5}$ Pa s, respectively. Furthermore, we used droplet impact visualisation data and experimental rheological data of a dilute polyethylene oxide (PEO) from Huh et al. [98]. Numerical simulations were conducted utilising the rheological properties of a dilute PEO fluid as described by [98] ($\rho_{\mathrm{f}} = 1000$ kg/m^3, $\eta_s = 0.001$ Pa s, $\eta_{\mathrm{p}} = 0.0013$ Pa s, $\lambda = 0.06$ s, and $\varepsilon = 0.85$). Huh et al. [98] experimented without nanoparticles at an impact velocity of 0.4 m/s. We simulated the impact of a dilute PEO fluid having $D_{d,o} = 3$ mm on a hydrophobic surface having $\theta = 106°$ at an initial impact velocity of 0.4 m/s, which corresponds to We of 7, Wi of 8, Ca of 7.76×10^{-3}, Oh of 0.003, and De of 7. We should point out that, given the lack of all of the rheological properties required for numerical simulation, we assumed part of the rheological properties. Hence, our simulation is not a perfect duplicate of the experimental work of Zang et al. [64] and

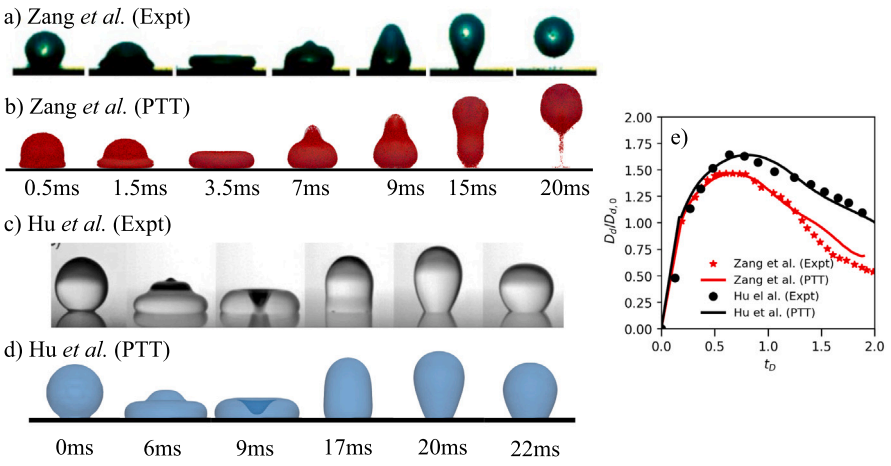

Fig. 2. (a–d) Comparison of the Zang et al. [64] experiment (with particles) and Huh et al. [98] (without particles) with numerical simulation in 3D. The red colour shows the distribution of particles within the fluid. The blue colour indicates the topology of the fluid droplet. The size of the nanoparticles was increased to enhance their visibility. (e) The temporal change of the normalised contact line diameter seen in [64,98] experiment with the results obtained from numerical simulations conducted using the PTT model.

Huh et al. [98]. In addition, we must acknowledge that errors occur during the execution of experiments, which may result in variances in the results. Notwithstanding this disparity, our findings closely align with experimental observation, as illustrated in Fig. 2 and simulation clip 1, which is appended in the supplemental information.

Fig. 2a,b demonstrates that the simulation and experimental measurements conducted by Zang et al. [64] exhibit an agreement, with only a slight disparity, at an initial impact velocity of 0.88 m/s. It should be noted that there is not a perfect match between the droplet's topology and the numerical simulation. However, the droplet's shape changes in the numerical simulation are similar to those observed in the experiment over time. This outcome is anticipated due to making certain assumptions about rheological properties. Fig. 2e demonstrates a strong correlation between the temporal changes in the contact line diameter and the experimental findings reported by Zang et al. [64] in their study. No evidence of nanoparticle aggregation or the formation of nanoparticle clusters was seen in the fluid. This outcome is anticipated due to the low concentration ($\phi = 10^{-5}$) and random distribution of the nanoparticles throughout the fluid. In simulation clip 1 of the supporting information, there is an alignment of the temporal fluctuations in the velocity of particles and viscoelastic fluid in the centre of the droplet. The simulation corresponds to $We = 30$, $Wi = 2640$, Ca of 4.6, Oh of 0.95, De of 30 and $Pe = 2.88 \times 10^7$. We estimated the dispersion coefficient of nanoparticles using the MSD method as 4.81×10^{-5} m^2/s. Fig. 2c,d demonstrates a substantial similarity between the experimental findings of Huh et al. [98] in the absence of particles and the numerical simulation conducted using the PTT model at an impact velocity of 0.4 m/s. Fig. 2e demonstrates a good match between the temporal change in the diameter of the contact line and the experimental findings Huh et al. (2015) [98] reported, with a slight disparity. The results show that a numerical model can be used to assess the dispersion of the nanoparticles following impact on a solid surface, despite some constraints associated with numerical simulation.

3.2. PTT and Oldroyd-B viscoelastic models and Newtonian fluid

We simulated the impact of a viscoelastic fluid droplet ($D_{d,0} = 0.002$ m) on a hydrophobic surface ($\theta = 120°$) having rheological properties of xanthan gum fluid similar to the ones presented by Campagnolo et al. [96] ($\eta_p = 0.08$, $\eta_s = 0.005$, $\lambda = 1.1$) using PTT-linear ($\varepsilon = 0.85$), PTT-exponential ($\varepsilon = 0.85$), and Oldroyld-B ($\varepsilon = 0$) models at an initial impact velocity of 0.8 m/s. Furthermore, we simulated the impact of Newtonian fluid on the hydrophobic surface, which has a viscosity of 0.08 Pa s. A total number of 100 soda-lime microspheres of 50 μm were randomly distributed in the droplets, resulting in a volume fraction ϕ of 0.0016 and indicating a dilute particle concentration in the fluid. The soda-lime microsphere had a density ρ_p of 2490 kg/m^3, a Young modulus E_p of 7.2×10^{10} N/m^2, and a Poisson's ratio χ_p of 0.20.

The spatiotemporal variation of a Newtonian fluid droplet differs greatly from that of a viscoelastic fluid droplet, as seen in Fig. 3. Fig. 3 and simulation clip 2 attached in the SI show that Newtonian fluid with constant viscosity μ of 0.08 Pa s could expand and recede without rebounding from the surface, whereas viscoelastic fluid with η_0 of 0.08 Pa s could expand and rebound from the surface during the receding phase. At a We value of 20, the maximal diameter of the droplet spreads in the viscoelastic fluid is 1.2 times greater than in the Newtonian fluid, at the same impact velocity $U_0 = 0.8$ m/s (see Fig. 3e). The maximum height of the droplet from the surface was less than the initial diameter of the droplet for Newtonian fluid, whereas viscoelastic fluid's maximum height was 1.4 times the initial diameter during the rebound phase of the droplet. The particles in the fluids follow the path adopted by the fluid's velocity field (see Fig. 3 and simulation clip 2 in the SI). The dispersion coefficient of particles, estimated using the MSD method, in Newtonian fluid and viscoelastic fluid were 1.83×10^{-6} m^2/s and 1.43×10^{-5} m^2/s, respectively, at the same Pe of 3.64×10^{11}.

In addition to surface tension forces that prevent fluid deformation, viscous forces predominate in Newtonian fluid due to its higher viscosity. On the contrary, viscoelastic fluid has shear thinning (viscosity decreases as shear rate increases) as well as elastic properties (relaxation of fluid after stretching or compression); thus, in high shear regions, the viscosity of the droplet decreases, resulting in less resistance to deformation of the droplet. This is the primary reason for the significant difference between Newtonian and viscoelastic fluids' droplet dynamics. In addition, viscoelastic fluids have a dispersion coefficient that is seven times greater than that of Newtonian fluids. This indicates that the shear-thinning property of viscoelastic fluids causes the particles to be more widely dispersed throughout the fluid.

In Fig. 3 and simulation clip 2 in the SI, we can see that we got identical results when we modelled the viscoelastic fluid with PTT-linear and PTT-exponential models (with an extensional parameter of $\varepsilon = 0.85$) and the Oldroyd fluid (with an extensional parameter of $\varepsilon = 0$). Both the PTT fluid and the Oldroyd-B fluid exhibit the same spatial variation in terms of droplet shape, diameter, height from the surface, and particle location in the fluid (see Fig. 3b,c,e,f). We compute the first normal stress difference ($N1 = \sigma_{xx} - \sigma_{yy}$) for both the PTT and Oldroyd-B fluids to conduct additional evaluations. Fig. 3 and simulation clip 2 in the SI demonstrate that the spatial and temporal variation in the local $N1$ is the same for PTT and Oldroyd-B fluids. The magnitude of

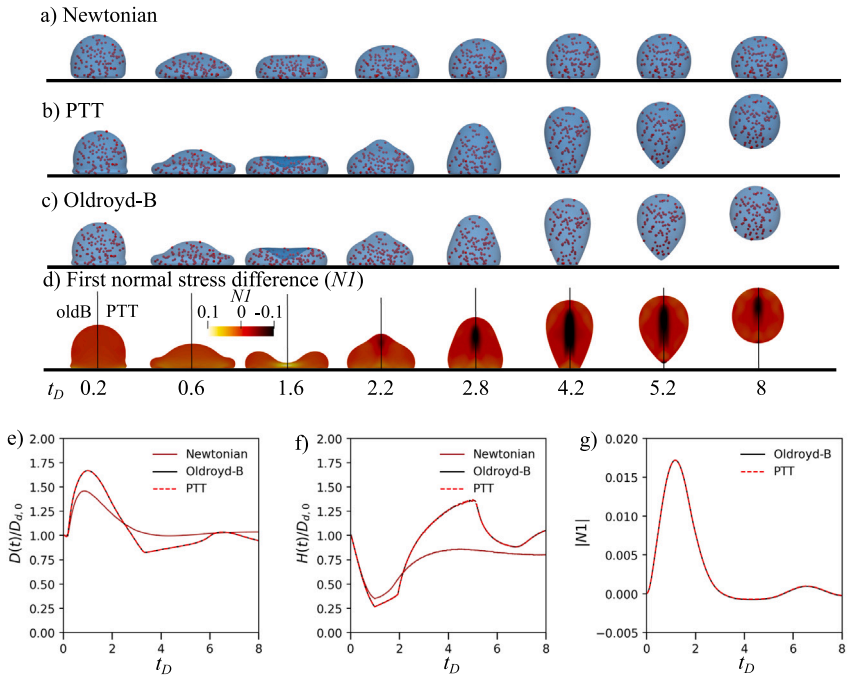

Fig. 3. Spatial variation in the droplet and micro-sphere particles dynamics (in 3D) during impact of (a) Newtonian fluid ($\mu = 0.08$) (b) viscoelastic PTT fluid ($\eta_p = 0.08$, $\eta_s = 0.01$, $\lambda = 1.1$, $\varepsilon = 0.85$), and (c) Oldroyd-B fluid ($\eta_p = 0.08$, $\eta_s = 0.01$, $\lambda = 1.1$) of ($D_{d,0} = 2$ mm) on a solid surface having a contact angle of 120° at $We = 20$, $Wi = 440$, $De = 440$, $Ca = 0.96$, $Oh = 0.21$, and $Pe = 3.64 \times 10^{11}$. (d) Comparison of the spatial variation of the local first normal stress difference ($N1$) with dimensionless time t_D at the centre of the droplet during the impact of Oldroyd-B fluid (left side) and PTT fluid (right side). Temporal variation of (e) the normalised droplet diameter ($D(t)/D_{d,0}$), (f) the normalised height of the droplet from the surface ($H(t)/D_{d,0}$), and (g) magnitude of the volume-averaged first normal stress difference $|N1|$.

the volume-averaged $|N1|$ with regard to the dimensionless time (t_D) is seen in Fig. 3g, further confirms this. The results show that the droplet impact dynamics are not considerably influenced by the extensional parameter ε, but are governed by the dominating rheological factors η_0, η_s, and λ. Therefore, the Oldroyd-B model, which is governed by only three rheological parameters (η_0, η_s, and λ), can be utilised for three-phase numerical simulations.

Shear stress controls the flow of Newtonian fluids, whereas polymers in viscoelastic non-Newtonian fluids cause normal stress. Hence, the first normal stress difference $N1$ experienced by the fluid determines the droplet impact dynamics. Fig. 3d and simulation clip 2 in the SI illustrate that the spatial distribution of $N1$ exhibits both positive and negative values, and it undergoes large temporal variations. The magnitude of the positive $N1$ is greater in regions where the fluid comes into contact with a solid surface. The highest positive $N1$ values are found at the outside edge of the solid–fluid contact line when the droplet is spreading and in the middle of the droplet when it is receding. The $N1$ values rise during the receding phase due to the collapse of the droplet's outer rim at the centre, followed by a subsequent rebound. During the rebounding process of the droplet, there is an observed augmentation of the negative $N1$ in the core region of the droplet. Fig. 3g demonstrates that the magnitude of $N1$ undergoes an increase during the spreading phase of the droplet and a subsequent decrease during the receding phase. The magnitude of $N1$ exhibits a modest increase during the detachment of the droplet from the surface, followed by a subsequent asymptotic decline. These findings suggest that the spatiotemporal variation in normal stress within the droplets is the primary factor influencing their behaviour.

The behaviour of the droplet impact is influenced by the volume fraction of the particles in the fluid. Consequently, we simulated a PTT fluid droplet impact at $U_0 = 0.8$ m/s utilising 10,000 randomly distributed particles having $d_p = 50$ μm. This yielded a volume fraction ϕ of 0.16. The mass of particles introduced into the 2 mm droplet was 1.63 mg, while the mass of the fluid droplet was 4.2 mg; therefore, the droplet containing 10,000 particles had a total mass of 5.83 mg. The initial total momentum of the droplet containing 10,000 particles was 4.65×10^{-6} kg m/s, whereas it was 3.36×10^{-6} kg m/s with 100 particles. Although the initial impact velocity of a fluid droplet remains constant, the results indicate that an increase in particle concentration causes the droplet's initial momentum to increase. As demonstrated in Fig. 4 and simulation clip 3 in the SI, we observed notably distinct droplet impact dynamics for viscoelastic fluids when impacting 100 and 10,000 particles, primarily due to differences in the initial momentum.

Fig. 4c demonstrates that the droplet's maximum spread with 10,000 particles was 1.2 times greater than that with 100 particles. The dimensionless time t_D of the spreading and receding phases was greater for the fluid containing 10,000 particles than that of 100 particles, as depicted in Fig. 4a–c. The volume-averaged total stress goes up during the spreading phase and down over time during the receding phase for both fluids with 100 and 10,000 particles, as shown in Fig. 4d. The PTT fluid containing 10,000 particles exhibits a greater total stress and for a longer duration when compared to the fluid with 100 particles. Fig. 4b displays the spatial distribution of the total stress (combination of normal and shear stress) magnitude within the droplet at various dimensionless time intervals. Fig. 4b clearly shows that the local total stress is maximum at the surface of the wall and the outside edge of the fluid–solid contact line during the spreading phase (at $t_D = 0.2$, 0.8). As the droplet spreads, it forms a thin layer of fluid around its centre, known as the lamella, and an outside rim that is taller than the lamella. As the spreading continues, the thin layer of lamella undergoes increased local stress and velocity in its core part (seen at $t_D = 1.4$, 2) due to polymer stretching in that specific area. The local total stress in the lamella region reduces as the droplet starts to recede. The local stresses are largely concentrated in the central region of the droplet and close to the wall's surface at the droplet's centre (i.e., along the axis of symmetry), observed at $t_D = 4$ during the receding and rebound phases. The periphery of the droplet suffers the lowest localised total stress.

The spatial distribution of particle velocity at various dimensionless times is illustrated in Fig. 4a. The velocity of the fluid and the

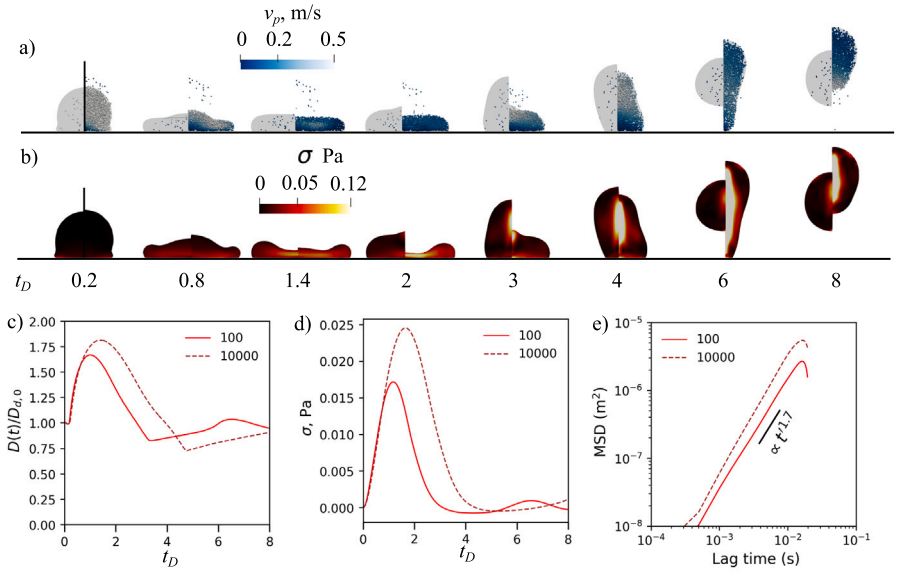

Fig. 4. Spatiotemporal variation of a) the particle velocity (v_p), b) the magnitude of the stress (σ) as a function of dimensionless time t_D during the impact of a PTT fluid droplet ($D_{d,0} = 2$ mm) on a solid surface having a contact angle of 120° at $We = 20$, $Wi = 440$, $Pe = 3.64 \times 10^{11}$ having 100 particles (left side) and 10000 particles (right side). Temporal variation of (c) the normalised droplet diameter ($D(t)/D_{d,0}$) and d) magnitude of the volume-averaged stress σ. (e) mean-square displacement (MSD) of particles. Short-time MSD is a function of $t'^{1.7}$, which suggests superdiffusive dispersion, as the black line indicates. The dispersion coefficients were 1.43×10^{-5} m^2/s and 2.82×10^{-5} m^2/s for droplets with 100 and 10000 particles, respectively. Fig. a) illustrates a cross-sectional view of a droplet at its central region in 3D, whereas Fig. (b) shows a 2D slice of the 3D domain at the centre of the droplet.

local velocity of the particles are identical. Consequently, advection governed the particle dispersion that occurred during droplet impact. Particles encountered their minimum velocity in the central region of the droplet, close to the solid surface, throughout the spreading phase. Most of their velocity was concentrated along the solid-fluid contact line (refer to $t_D = 0.4$, 0.8). The velocity in the lamella region begins to increase as the droplet expands further and reaches its minimum value when it reaches its maximal spread. When droplets begin to recede, the outer rims collapse with each other at the centre, resulting in the droplet's interior experiencing the greatest pressure. Consequently, a Worthington jet is formed, which causes an elevation in both the fluid velocity and particle velocity within the upper core region of the droplet (refer to $t_D = 3$, 4). The momentum concentration in the uppermost region of the droplet's core is significantly greater than the surface tension forces between the solid and fluid, resulting in the droplet's eventual rebound from the surface. Because the momentum and velocity of the particles in the fluid are comparable to those of the fluid itself, the particles in the fluid travel with the fluid and exhibit a distribution of velocities that is similar to the fluid's.

The mean square displacement of particles upon droplet impact on a hydrophobic surface with fluid containing 100 particles and 10,000 particles is depicted in Fig. 4e. The MSD for both fluids shows a non-linear relationship with a lag-time, as shown in Fig. 4e. The MSD curve of a fluid containing 100 particles differs from that of a fluid containing 10,000 particles. The dispersion coefficients obtained using the MSD approach were 1.43×10^{-5} m^2/s and 2.82×10^{-5} m^2/s for droplets with 100 and 10,000 particles, respectively, at the same Pe of 3.64×10^{11}. The short-time MSD $\propto t'^{1.7}$ exhibits a non-Fickian super-diffusive dispersion. The main reason for a non-Fickian super-diffusive dispersion of particles within a viscoelastic fluid is the large spatial fluctuation of the fluid velocity with time (see Fig. 4a).

3.3. Influence of wettability on normal and shear stresses

The impact behaviour of droplets can be affected by variations in the fluid's rheological characteristics, the particles' size and density, and the surface's wettability. Most biofluids are dilute viscoelastic fluids with a viscosity slightly higher than their solvent (i.e., water). Silica nanoparticles are frequently employed in numerous industrial and biological applications. As a result, we simulated the impact of a dilute polyethylene oxide droplet ($D_{d,0} = 0.001$ m) containing 5,000 silica nanoparticles on hydrophobic ($\theta = 120°$) and hydrophilic ($\theta = 30°$) surfaces over a Pe (5.91×10^5 - 1.18×10^8). This corresponds to a volume fraction (ϕ) of 4×10^{-11}. These simulations correspond to Weber numbers We ranging from 0.001 to 60, Weissenberg numbers Wi ranging from 0.06 to 120, Deborah numbers De ranging from 0.06–120, Capillary numbers Ca ranging from 1.94×10^{-4} to 3.88×10^{-2} and Ohnesorge number Oh 0.005.

Numerical simulations were conducted utilising the rheological properties of a PEO fluid as described by Huh et al. [98] ($\rho_f = 1000$ kg/m^3, $\eta_s = 0.001$ Pa s, $\eta_p = 0.0013$ Pa s, $\lambda = 0.06$ s, and $\varepsilon = 0.85$). At the beginning of the simulation, a dilute PEO droplet with a diameter of $D_{d,0} = 0.001$ m was randomly distributed with silica nanoparticles ($\rho_p = 2000$ kg/m^3, $E_p = 1.1 \times 10^{10}$ N/m^2, $\chi_p = 0.16$ [88]) of $d_p = 20$ nm.

Fig. 5 and Fig. 6 depict the changes in droplet shape, the velocity of nanoparticles (v_p), fluid velocity (u_f), normal stress along the XX and YY directions (σ_{XX}, σ_{YY}), and shear stress along the XY direction (σ_{XY}) during the impact of a dilute viscoelastic fluid droplet with a diameter of 1 mm on both a hydrophilic surface with a contact angle of $\theta = 30°$ (Fig. 5) and a hydrophobic surface with a contact angle of $\theta = 120°$ (Fig. 6). These figures expressly represent the spatiotemporal variation of these parameters for a Weber number (We) of 4, a Péclet number (Pe) of 2.96×10^7 and Weissenberg number (Wi) of 30. The diameter of the droplet's spread is 2.3 times larger for an angle of $\theta = 30°$ compared to an angle of $\theta = 120°$. This outcome is anticipated since a hydrophilic surface has the ability to retain fluid in contact with the solid surface for an extended period of time. The droplet underwent a process of spreading, receding, rebounding, and detaching from the surface, with an angle of $\theta = 120°$. As anticipated, a droplet with an angle of $\theta = 30°$ exhibited spreading, receding, and maintained adhesion to the surface.

The velocity distribution of nanoparticles exhibits a resemblance to the velocity of the dilute viscoelastic fluid across various dimensionless time t_D (see Figs. 5 and 6). This similarity implies that the fluid's velocities predominantly influence the motion of the nanoparticles within the fluid during droplet impact at $\theta = 30°$ and $\theta = 120°$ and at We of 4 and Wi of 30. The velocity of both the fluid and nanoparticles

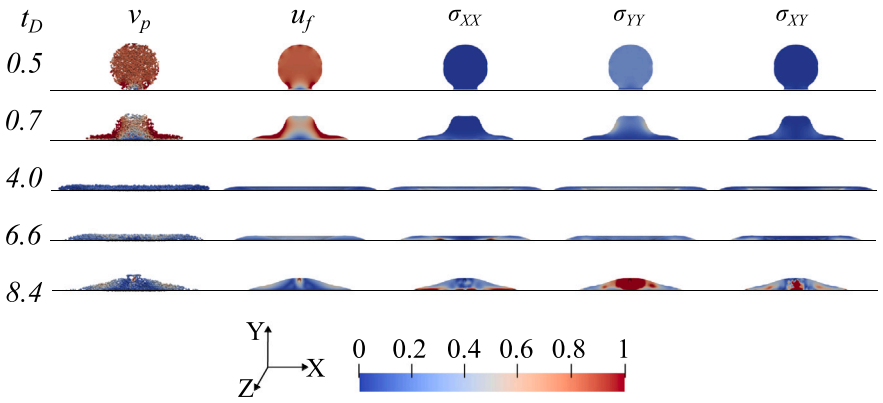

Fig. 5. Spatiotemporal variation of the nanoparticles velocity (v_p), fluid velocity (u_f), normal stress along XX direction (σ_{XX}), normal stress along YY direction (σ_{YY}), shear stress along XY direction (σ_{XY}) over a range of dimensionless time t_D during the impact of a PEO fluid droplet ($D_{d,0} = 1$ mm) on a solid surface having a contact angle of 30° at *We* = 4, *Pe* = 2.96×10^7 and *Wi*. The colour bar visually represents the normalised profile of parameters relative to their respective maximum values. The Fig. illustrates a cross-sectional view of a droplet at its central region in 3D.

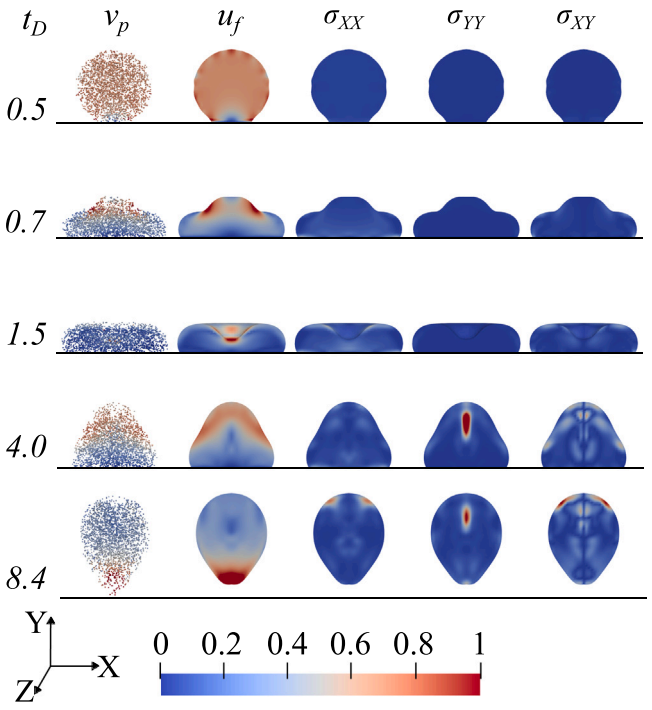

Fig. 6. Spatiotemporal variation of the nanoparticles velocity (v_p), fluid velocity (u_f), normal stress along XX direction (σ_{XX}), normal stress along YY direction (σ_{YY}), shear stress along XY direction (σ_{XY}) over a range of dimensionless time t_D during the impact of a PEO fluid droplet ($D_{d,0} = 1$ mm) on a solid surface having a contact angle of 120° at *We* = 4, *Pe* = 2.96×10^7 and *Wi*. The colour bar visually represents the normalised profile of parameters relative to their respective maximum values. The Fig. illustrates a cross-sectional view of a droplet at its central region in 3D.

exhibits its highest magnitude in proximity to the air–water interface, in contrast to the central region of the droplet, across a range of t_D. The predominant concentration of high fluid velocities occurs primarily within the region where the droplet undergoes morphological changes. The histogram of the velocity field within a viscoelastic fluid droplet at $t_D = 1.5$ is depicted in Fig. 7c,d. The relative frequency of velocity distribution along the X and Z directions exhibits overlap and symmetry around zero velocity while being non-Gaussian for both $\theta = 30°$ and $\theta = 120°$. The relative frequency of velocity distribution along the Y-direction exhibits a skewed profile in the negative direction at an angle of $\theta = 30°$, which can be attributed to the channelised flow of fluid in the negative Y-direction. In contrast, the velocity distribution exhibits a non-Gaussian profile with a predominant skewness in the positive Y-direction for $\theta = 120°$. This can be attributed to the channelised flow of fluid in both positive and negative Y-directions during the spreading phase.

Figs. 5 and 6 show that normal stress along the XX direction (σ_{XX}) is predominantly high near the boundary region of the droplet, specifically at the solid surface, due to friction between the solid and fluid during the spreading and receding phases. In contrast, normal stress along the YY direction (σ_{YY}) is predominately high near the boundary during the spreading phase, in the top central region, and in certain pockets of boundary regions during the receding/rebounding phase. The region shown in Figs. 5 and 6 with higher values of σ_{XX} and σ_{YY} is the region where maximum stretching and compression of the elastic polymer molecules occurs.

For both $\theta = 30°$ and $\theta = 120°$, the normal stress distribution along XX, YY, and ZZ (σ_{XX}, σ_{YY}, σ_{ZZ}) shows a non-Gaussian skewed profile in the positive direction (see Fig. 7a). Fig. 7a illustrates the overlapping of the histogram of distribution of σ_{XX} and σ_{ZZ} and exhibiting a bimodal distribution with two distinct peaks for both $\theta = 30°$ and $\theta = 120°$ at $t_D = 1.5$. The presence of these two peaks suggests the existence of two distinct regions characterised by elevated normal stress values along the XX and ZZ directions. The first peak corresponds to the values of σ_{XX} and σ_{ZZ} within and close to the air–water interface droplet, while the second peaks, characterised by significantly higher values, represent the values at the fluid–solid interface. The magnitudes of σ_{XX} and σ_{ZZ} at $\theta = 30°$ are 6.4 times greater than those at $\theta = 120°$. In contrast, the magnitude of σ_{YY} is > 15 times greater for $\theta = 120°$ compared to $\theta = 30°$. Based on these findings, it appears that the normal stress σ_{XX} and σ_{ZZ} dominate when a viscoelastic fluid impacts a hydrophilic surface at $t_D = 1.5$, while the normal stress σ_{YY} dominates when a droplet impacts a hydrophobic surface at $t_D = 1.5$. At $\theta = 30°$, we find that the magnitudes of σ_{XX} and σ_{ZZ} are larger than the magnitude of σ_{YY} during the spreading and receding phases. At $\theta = 120°$, the magnitudes of σ_{XX} and σ_{ZZ} are greater compared to the magnitude of σ_{YY} during the spreading phase, whereas the magnitude of σ_{YY} is greater compared to the magnitudes of σ_{XX} and σ_{ZZ} during the receding and rebounding phases.

The histogram of the distribution of shear stress along the XY, XZ, and YZ directions (σ_{XY}, σ_{XZ}, σ_{YZ}) demonstrates overlap and symmetry around zero shear stress while exhibiting non-Gaussian characteristics for both $\theta = 30°$ and $\theta = 120°$ (see Fig. 7b). The average normal stress within the droplet is three orders of magnitude higher than the average shear stress for both contact angles of 30 degrees and 120 degrees. This observation suggests that normal stress plays a dominant role in

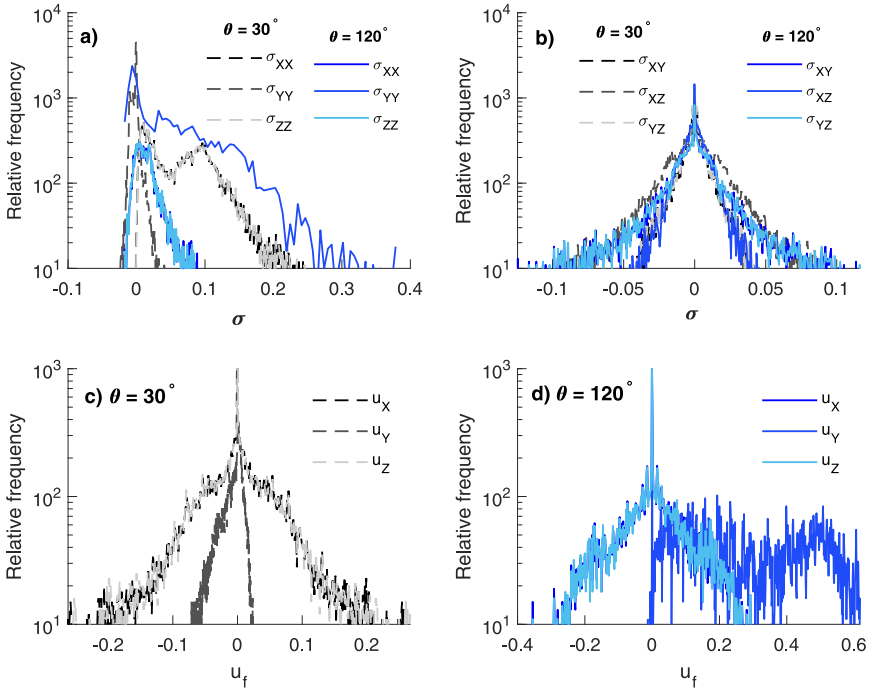

Fig. 7. Histogram of the distribution of (a) the normal stress (σ_{XX}, σ_{YY}, σ_{ZZ}) along XX, YY, and ZZ directions, (b) the shear stress (σ_{XY}, σ_{XZ}, σ_{YZ}) along XY, XZ and YZ directions, (c), (d) the fluid velocity (u_X, u_Y, u_Z) along X, Y, and Z directions, respectively, during an impact of PEO fluid droplet on a solid surface having $\theta = 30°$ and $\theta = 120°$ at $t_D = 1.5$ [$We = 4$, $Pe = 2.96 \times 10^7$ and $Wi = 30$].

influencing both the viscoelastic droplet's morphology and the flow of the fluid.

The fluid droplet can be characterised as a dilute viscoelastic fluid, exhibiting a viscosity (0.0013 Pa s) that is marginally greater than that of water (0.001 Pa s). The velocity of a Newtonian fluid shows spatiotemporal variation primarily due to the influence of shear stress [11]. In contrast, for a viscoelastic fluid, the fluid velocity is primarily governed by normal stresses [11,22]. The observed behaviour of nanoparticles migrating within a viscoelastic fluid, which is similar to the fluid velocity, is depicted in Figs. 5 and 6. These figures, namely Fig. 5 (for $\theta = 30°$), Fig. 6 (for $\theta = 120°$), Fig. 7 (for a histogram of the distribution of stresses and velocity), provide clear evidence that the dispersion of nanoparticles is primarily influenced by the normal stress within the viscoelastic fluid. These results agree with experimental results obtained by Babayekhorasani et al. [45] and Jacob et al. [95] for the dispersion of nanoparticles in porous media.

3.4. Droplets maximum spread

The time-dependent spread of the droplet diameter over a range of Péclet numbers (5.91×10^5–1.18×10^8) and Weissenberg numbers (0.6–120) is illustrated in Fig. 8. The maximum diameter of the droplet's spread shows an increase with an increase in *Pe* and *Wi* (see Fig. 8). The maximum spread diameter is influenced by wettability, with a higher value observed for the hydrophilic surface ($\theta = 30°$) compared to the hydrophobic surface ($\theta = 120°$). At $\theta = 30°$, the maximum spread is > 1.6 times than that at $\theta = 120°$. The rebounding of droplet impact at an angle of 30° was not observed in our study. However, we did observe droplets rebounding at an angle of 120° when the Péclet number (*Pe*) exceeded 2.96×10^7, the Weber number (*We*) exceeded 4 and *Wi* exceeded 30. These results agree with the results of Hu et al. [32] and Aksoy et al. [99]. Fig. 8c and 8d demonstrate that the maximum spread of the droplet exhibits a comparable pattern with respect to both the Péclet number (*Pe*) and the Weissenberg number (*Wi*).

3.5. Nanoparticle dispersion

The mean square displacement (MSD) method was employed to assess the dispersion of nanoparticles within a viscoelastic fluid [29,45,95] during droplet impact. Fig. 9a demonstrates that the mean squared displacement exhibits a non-linear relationship with lag-time for a range of *Pe* and *Wi* at contact angles $\theta = 30°$ and $\theta = 120°$. The data presented in Fig. 9 demonstrates that the MSD over a short time is $\propto t'^{1.82}$ for both $\theta = 30°$ and $\theta = 120°$ across various values of the *Pe* and *Wi*. The exponent of 1.82 indicates that nanoparticles exhibit a non-Fickian superdiffusive dispersion process [53] when subjected to droplet impact on a solid surface across a range of *Pe* (5.91×10^5 – 1.18×10^8) and Weissenberg number, *Wi* (0.6 - 120). Fig. 9a illustrates that the MSD for $\theta = 30°$ exhibits a slight increase as the Péclet number (*Pe*) increases. Nevertheless, the MSD at an angle of $\theta = 120°$ exhibits a significantly low value for $Pe < 5.91 \times 10^6$, followed by a sudden and substantial increase in MSD for $Pe > 5.91 \times 10^6$, with a slight subsequent increase for $Pe > 5.91 \times 10^7$.

Fig. 9c and 9d demonstrate a nonlinear relationship between the normalised dispersion coefficient (D/D_{SE}) and the Péclet number and the Weissenberg number for both $\theta = 30°$ and $\theta = 120°$. The dispersion of nanoparticles exhibits greater magnitude at a contact angle of $\theta = 120°$ in comparison to $\theta = 30°$ when the Péclet number exceeds 5.91×10^7, and the Weissenberg number exceeds 6. The findings of this study indicate that the dispersion of nanoparticles in a viscoelastic fluid is influenced by wettability, the *Pe*, and the *Wi*. The variation in dispersion, influenced by wettability, can be attributed to the differences in normal stress at $\theta = 30°$ and $\theta = 120°$ in both space and time. The normalised velocity autocorrelation function (VACF) is depicted in Fig. 9b across a spectrum of *Pe* and θ values. The velocity autocorrelation function exhibits a positive correlation across a spectrum of *Pe* and θ. The primary factor influencing the migration of nanoparticles during droplet impact is the advection of the fluid. Consequently, a significant proportion of the nanoparticles tend to align themselves with the direction of fluid flow. This phenomenon positively correlates the *Pe* and VACF over θ.

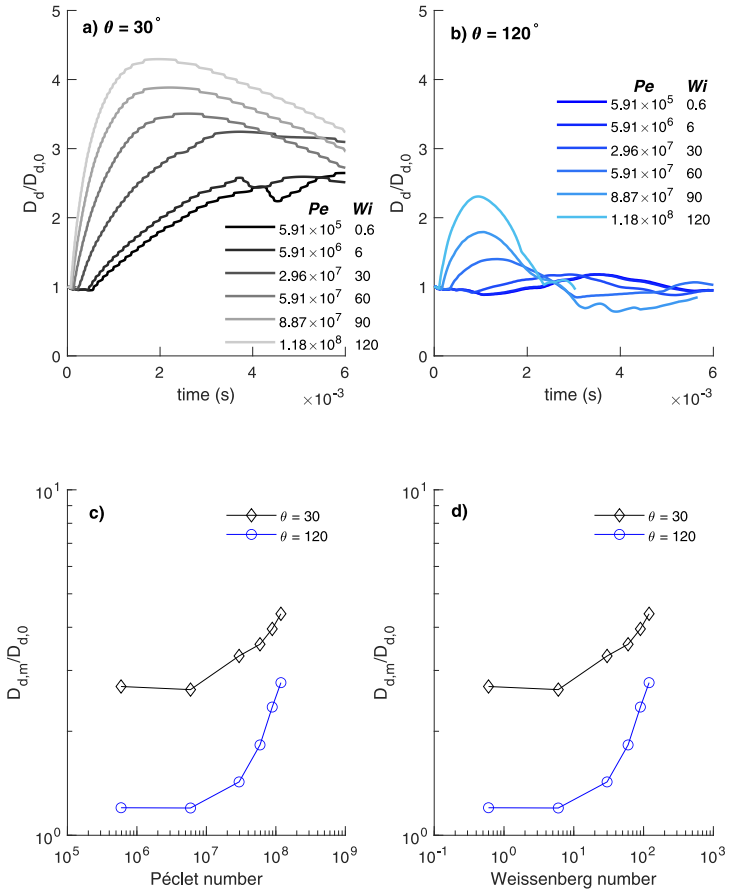

Fig. 8. Temporal variation of droplet diameter (D_d) with respect to its initial diameter ($D_{d,0}$) at a) $\theta = 30°$ (b) $\theta = 120°$ over a range of *Pe* and *Wi*. Maximum spread of the droplet diameter ($D_{d,m}$) as a function of (c) Péclet number *Pe* and d) Weissenberg number *Wi*. The legend shows that the intensity of the legend colour decreases with an increase in *Pe*.

The histogram of the distribution of nanoparticle velocities in the X, Y, and Z directions, relative to the average velocity of all nanoparticles within the examined domains, is depicted in Fig. 10. The velocity distributions of nanoparticles along the X and Z directions demonstrate a lack of overlap, displaying symmetry around zero velocity and adhering to a non-Gaussian distribution for both $\theta = 30°$ and $\theta = 120°$ across a range of *Pe* and *Wi*. Nevertheless, the velocity distribution of nanoparticles in the Y-direction exhibits a non-Gaussian skewness, characterised by a bimodal distribution with two distinct peaks for both $\theta = 30°$ and $\theta = 120°$. The velocity distribution exhibits one peak at approximately zero velocity for both angles of $\theta = 30°$ and $\theta = 120°$. Nonetheless, a second peak can be detected in the negative direction when θ is equal to 120°, *Pe* exceeds 2.96×10^7 and *Wi* exceeds 30. Similarly, a second peak can be observed in the positive direction when θ is equal to 30°, *Pe* is less than 2.96×10^7 and *Wi* is less than 30. These results indicate that the dispersion of nanoparticles exhibits a non-Fickian transport process when suspended in a dilute viscoelastic fluid, and this behaviour is influenced by the wettability of the viscoelastic fluid with a solid surface.

4. Conclusion

Integrating RheoTool's [65] volume-of-fluid approach with OpenFOAM's Lagrangian library, we developed a volume-of-fluid-Lagrangian method to model the transport of nanoparticles in a viscoelastic fluid with three phases: particles, air, and fluid. We simulated the impact of a particle-laden viscoelastic fluid droplet on a hydrophobic solid surface using the Phan-Thien-Tanner (PTT) model and compared it with the Oldroyd-B model and Newtonian fluid. The results show statistically insignificant variation in droplet dynamics with the PTT and Oldroyd models. Thus, the rheological parameters zero shear viscosity (η_0), polymeric viscosity (η_p), and relaxation time (λ) of a viscoelastic fluid play a governing role in droplet dynamics as compared to the extensibility parameter ϵ during droplet impact. The droplet dynamics of Newtonian fluid were significantly different than those of the PTT model at the same Weber number; unlike Newtonian droplets, viscoelastic droplets could rebound from the surface. Shear thinning, where the viscosity decreases as the shear stress increases, is the primary reason for the viscoelastic droplet's rebound. Due to its constant viscosity, the Newtonian fluid exhibited greater deformation resistance than the viscoelastic fluid. Therefore, the dispersion of nanoparticles in a viscoelastic fluid was seven times higher than in a Newtonian fluid. It was observed that the initial momentum of droplet impact increases with the volume fraction of particles in the viscoelastic fluid, even when the initial impact velocity remains constant. This increase in the initial momentum leads to different droplet impact dynamics and the dispersion of particles.

We simulated the impact of a dilute viscoelastic fluid on hydrophobic and hydrophilic solid surfaces over a range of *Pe*. The spatiotemporal variation of nanoparticle velocity within a viscoelastic fluid resembled the spatiotemporal variation of fluid velocity during the impact of a viscoelastic droplet on a hydrophilic and hydrophobic surface, suggesting that nanoparticle transport is advection-dominated. We observed that the spatial and temporal variation in the first normal stress difference (which has positive and negative components) in the viscoelastic fluid during droplet impact governs the fluid's velocity field and deformation of the droplet topology, along with viscous and surface tension forces. The magnitude of normal stress during droplet impact was three orders of magnitude greater than shear stress. Consequently, the normal stress field in the droplet dictates the particle's trajectory in the viscoelastic fluid during droplet impact. We observed the non-Gaussian distribution of the particle's velocity, fluid velocity, fluid's

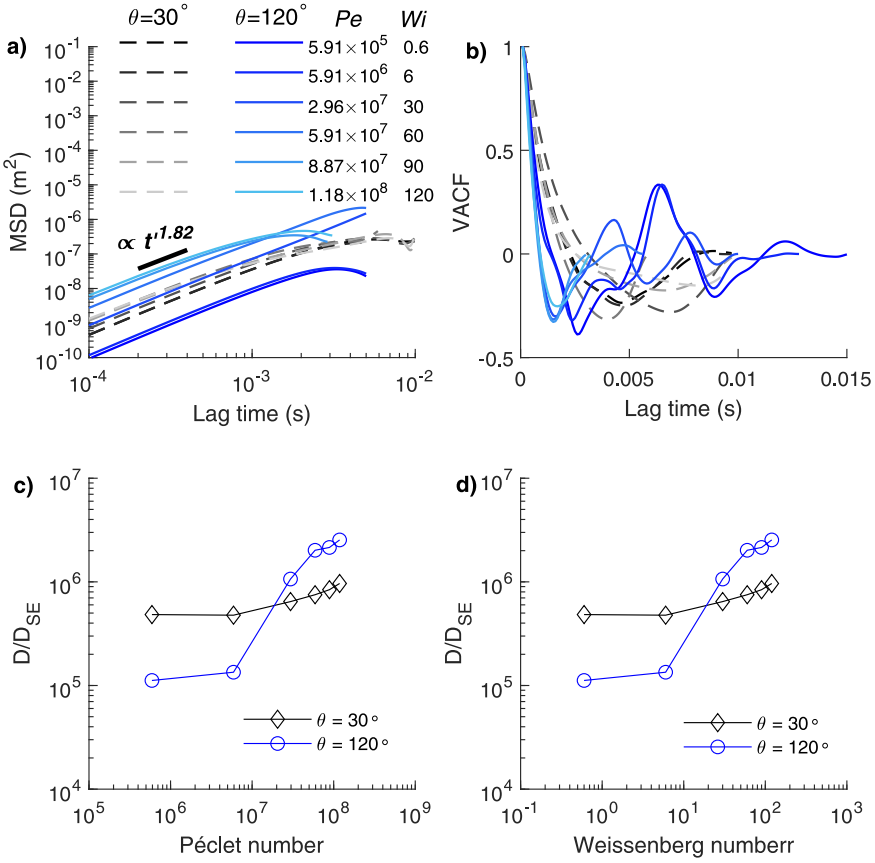

Fig. 9. (a) Mean-square displacement (MSD) (b) normalised velocity autocorrelation function (VACF) over a range of *Pe* and *Wi*. Normalised dispersion coefficient (D/D_{SE}) of nanoparticles over a range of (c) Péclet number (*Pe*) and d) Weissenberg number (*Wi*) during the impact of dilute PEO fluid on a solid surface having $\theta = 30°$ and $\theta = 120°$. Short-time MSD is a function of $t'^{1.82}$, which suggests superdiffusive dispersion, as the black line indicates. The legend shows that the intensity of the legend colour decreases with an increase in *Pe*.

normal stress, and fluid's shear stresses. This spatial and temporal variation of the overall stresses in the viscoelastic fluid leads to the advection-dominated non-Fickian transport process of nanoparticles in a viscoelastic fluid.

The intricate behaviour of viscoelastic fluid at the solid interface depends on various factors, such as the material properties of the solvent, the concentrations of polymers within the solvent, the presence of additional chemical compounds, and the molecular interactions between the fluid and the solid surface. Dynamic contact angles can be observed in many viscoelastic fluids, leading to Navier slips at the solid boundary. Moreover, it is worth noting that the scaling behaviour of the drag coefficient in a viscoelastic fluid exhibits considerable variations compared to that of a Newtonian fluid [9,10,26,100]. In the future, we plan to examine the effects of dynamic contact angle, Navier slip, and changes in drag coefficient on the dispersion of particles and the dynamics of contact lines created by particle-laden viscoelastic droplets impacting solid surfaces with varying degrees of curvature.

CRediT authorship contribution statement

Takshak Shende: Writing – review & editing, Writing – original draft, Visualization, Validation, Software, Methodology, Investigation, Conceptualization. **Ian Eames:** Writing – review & editing, Supervision, Project administration, Methodology, Funding acquisition, Conceptualization. **Mohammad Hadi Esteki:** Writing – review & editing, Writing – original draft, Investigation. **Yousef Javanmardi:** Writing – review & editing, Writing – original draft, Software, Investigation. **Emad Moeendarbary:** Writing – review & editing, Writing – original draft, Validation, Supervision, Software, Resources, Project administration, Conceptualization.

Declaration of competing interest

The authors declare that they have no known competing financial interests or personal relationships that could have appeared to influence the work reported in this paper.

Data availability

Data will be made available on request.

Acknowledgements

TS, IE, MHE, and EM are grateful for the Engineering and Physical Sciences Research Council grant (EP/W009889/1). We acknowledge using the University College London (UCL) Kathleen High-Performance Computing Facility (Kathleen@UCL) and associated support services to complete this work.

Appendix A. Supplementary information

1. Simulation movie Clip 1: Spatiotemporal variation of the fluid's velocity field and particle's velocity field during an impact of a PTT fluid droplet with 10^6 nanoparticles on a surface having $\theta = 160°$ at an impact velocity 0.88 m/s and *We* of 30
2. Simulation movie Clip 2: Spatiotemporal variation of the first normal stress difference $N1$ field during an impact of a Newtonian fluid, Oldroyd-B fluid and PTT fluid with 100 micro-sphere particles on a surface having $\theta = 120°$ and *We* of 20.

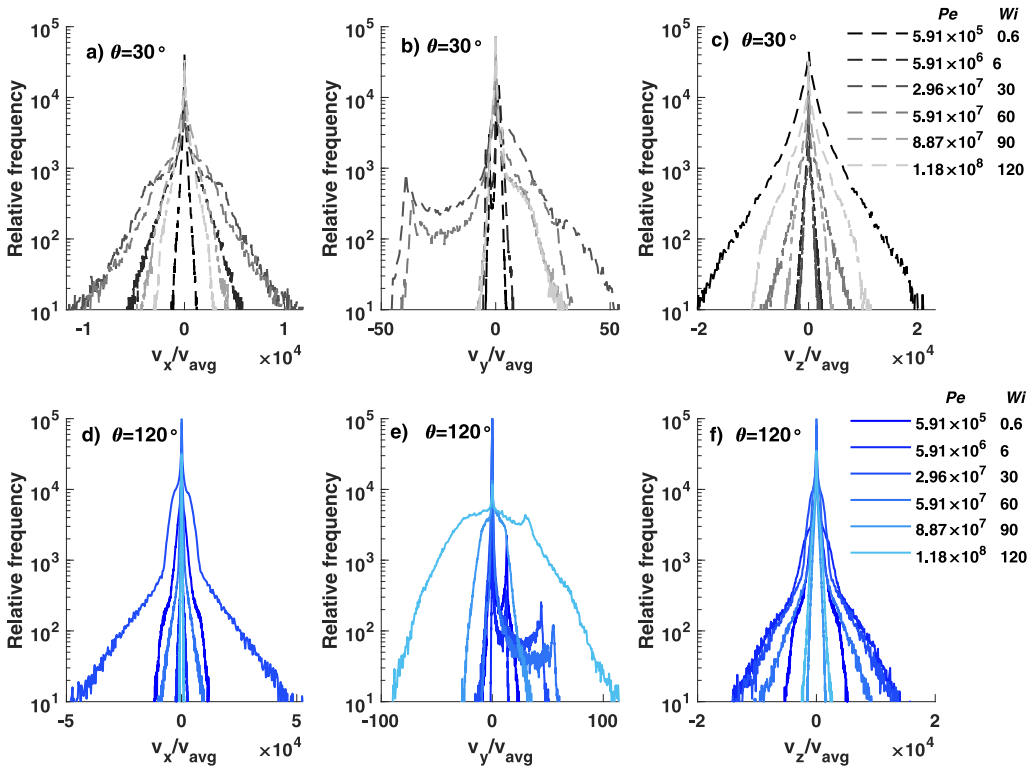

Fig. 10. Histogram of the distribution of the nanoparticle velocity (v_X, v_Y, v_Z) field along X, Y, and Z directions during the impact of PEO fluid on a solid surface having $\theta = 30°$ and $\theta = 120°$ over a range of *Pe* and *Wi*. The average velocity of the nanoparticle in that direction is used to normalise the particle's velocity.

3. Simulation movie Clip 3: Spatiotemporal variation of the velocity field and the magnitude of stress σ field during an impact of a PTT fluid droplets with 100 and 10000 micro-sphere particles on a surface having $\theta = 120°$ and *We* of 20.
4. Validation of a PTT rheological model.

References

[1] I. Eames, F. D'Aiuto, S. Shahreza, Y. Javanmardi, R. Balachandran, M. Hyde, Y.-L. Ng, K. Gulabivala, S. Watson, H. Davies, et al., Removal and dispersal of biofluid films by powered medical devices: Modeling infectious agent spreading in dentistry, Iscience 24 (11) (2021).

[2] J. Lacey, J. Dutkiewicz, Bioaerosols and occupational lung disease, J. Aerosol Sci. 25 (8) (1994) 1371–1404.

[3] R. Skalak, N. Ozkaya, T.C. Skalak, Biofluid mechanics, Annu. Rev. Fluid Mech. 21 (1) (1989) 167–200.

[4] J. Fine, Applied Biofluid Mechanics, McGraw-Hill Education, 2017.

[5] K.B. Chandran, S.E. Rittgers, A.P. Yoganathan, Biofluid Mechanics: The Human Circulation, CRC Press, 2006.

[6] K.G. Kornev, A.V. Neimark, Modeling of spontaneous penetration of viscoelastic fluids and biofluids into capillaries, J. Colloid Interface Sci. 262 (1) (2003) 253–262.

[7] M.A. Alves, P.J. Oliveira, F.T. Pinho, A convergent and universally bounded interpolation scheme for the treatment of advection, Internat. J. Numer. Methods Fluids 41 (1) (2003) 47–75.

[8] S.S. Datta, A.M. Ardekani, P.E. Arratia, A.N. Beris, I. Bischofberger, G.H. McKinley, J.G. Eggers, J.E. López-Aguilar, S.M. Fielding, A. Frishman, et al., Perspectives on viscoelastic flow instabilities and elastic turbulence, Phys. Rev. Fluids 7 (8) (2022) 080701.

[9] S. Faroughi, C. Fernandes, J.M. Nóbrega, G. McKinley, A closure model for the drag coefficient of a sphere translating in a viscoelastic fluid, J. Non-Newton. Fluid Mech. 277 (2020) 104218.

[10] C. Fernandes, S. Faroughi, R. Ribeiro, A. Isabel, G. McKinley, Finite volume simulations of particle-laden viscoelastic fluid flows: Application to hydraulic fracture processes, Eng. Comput. 38 (6) (2022) 5395–5421.

[11] R.B. Bird, R.C. Armstrong, O. Hassager, Fluid Mechanics, Dynamics of Polymeric Liquids, vol. 1, New York: Wiley, 1987.

[12] O. Ayar, C. Fernandes, L. Ferrás, M. Alves, Numerical simulations of suspensions of rigid spheres in shear-thinning viscoelastic fluids, Phys. Fluids 35 (11) (2023).

[13] A. Zhang, E.S. Shaqfeh, Rheology of non-Brownian particle suspensions in viscoelastic solutions. Part 1: Effect of the polymer concentration, J. Rheol. 67 (2) (2023) 499–516.

[14] M. Wang, Y. Feng, D. Owen, T. Qu, A novel algorithm of immersed moving boundary scheme for fluid–particle interactions in DEM–LBM, Comput. Methods Appl. Mech. Engrg. 346 (2019) 109–125.

[15] Y.K. Lee, K.H. Ahn, A novel lattice Boltzmann method for the dynamics of rigid particles suspended in a viscoelastic medium, J. Non-Newton. Fluid Mech. 244 (2017) 75–84.

[16] S. Qin, M. Jiang, K. Ma, J. Su, Z. Liu, Fully resolved simulations of viscoelastic suspensions by an efficient immersed boundary-lattice Boltzmann method, Particuology 75 (2023) 26–49.

[17] K. Höfler, S. Schwarzer, Navier-Stokes simulation with constraint forces: Finite-difference method for particle-laden flows and complex geometries, Phys. Rev. E 61 (6) (2000) 7146.

[18] A. Perrin, H.H. Hu, An explicit finite-difference scheme for simulation of moving particles, J. Comput. Phys. 212 (1) (2006) 166–187.

[19] G. D'Avino, P.L. Maffettone, Numerical simulations on the dynamics of a particle pair in a viscoelastic fluid in a microchannel: Effect of rheology, particle shape, and confinement, Microfluid. Nanofluid. 23 (2019) 1–14.

[20] A. Vázquez-Quesada, M. Ellero, SPH modeling and simulation of spherical particles interacting in a viscoelastic matrix, Phys. Fluids 29 (12) (2017).

[21] T. Shende, D. Mangal, J.C. Conrad, V. Niasar, M. Babaei, Nanoparticle transport within non-Newtonian fluid flow in porous media, Phys. Rev. E 106 (1) (2022) 015103.

[22] M.A. Alves, P.J. Oliveira, F.T. Pinho, Numerical methods for viscoelastic fluid flows, Annu. Rev. Fluid Mech. 53 (2021) 509–541.

[23] N. Thien, R.I. Tanner, A new constitutive equation derived from network theory, J. Non-Newton. Fluid Mech. 2 (4) (1977) 353–365.

[24] J.G. Oldroyd, On the formulation of rheological equations of state, Proc. R. Soc. Lond. Ser. A Math. Phys. Sci. 200 (1063) (1950) 523–541.

[25] H. Giesekus, A simple constitutive equation for polymer fluids based on the concept of deformation-dependent tensorial mobility, J. Non-Newton. Fluid Mech. 11 (1–2) (1982) 69–109.

[26] S.A. Faroughi, A.I. Roriz, C. Fernandes, A meta-model to predict the drag coefficient of a particle translating in viscoelastic fluids: A machine learning approach, Polymers 14 (3) (2022) 430.

[27] A. Zhang, E.S. Shaqfeh, Rheology of non-Brownian particle suspensions in viscoelastic solutions. Part II: Effect of a shear thinning suspending fluid, J. Rheol. 67 (2) (2023) 517–540.

[28] M. Yang, S. Krishnan, E.S. Shaqfeh, Numerical simulations of the rheology of suspensions of rigid spheres at low volume fraction in a viscoelastic fluid under shear, J. Non-Newton. Fluid Mech. 233 (2016) 181–197.

[29] T. Shende, V. Niasar, M. Babaei, Pore-scale simulation of viscous instability for non-Newtonian two-phase flow in porous media, J. Non-Newton. Fluid Mech. 296 (2021) 104628.

[30] N.H. Pham, D.V. Papavassiliou, Nanoparticle transport in heterogeneous porous media with particle tracking numerical methods, Comput. Part. Mech. 4 (1) (2017) 87–100.

[31] H. Almohammadi, A. Amirfazli, Droplet impact: Viscosity and wettability effects on splashing, J. Colloid Interface Sci. 553 (2019) 22–30.

[32] M. Hu, J. Zhou, Y. Li, X. Zhuo, D. Jing, Effects of the surface wettability of nanoparticles on the impact dynamics of droplets, Chem. Eng. Sci. 246 (2021) 116977.

[33] Z. Hu, X. Zhang, S. Gao, Z. Yuan, Y. Lin, F. Chu, X. Wu, Axial spreading of droplet impact on ridged superhydrophobic surfaces, J. Colloid Interface Sci. 599 (2021) 130–139.

[34] R. Zhao, M. Yu, Z. Sun, L.-j. Li, X.-y. Guo, Y. Xu, X.-m. Wu, Regulating droplet impact and wetting behaviors on hydrophobic leaves using a nonionic surfactant, J. Colloid Interface Sci. 629 (2023) 926–937.

[35] Y. Wang, Y. Wang, S. Wang, Droplet impact on cylindrical surfaces: Effects of surface wettability, initial impact velocity, and cylinder size, J. Colloid Interface Sci. 578 (2020) 207–217.

[36] Y.T. Aksoy, Y. Zhu, P. Eneren, E. Koos, M.R. Vetrano, The impact of nanofluids on droplet/spray cooling of a heated surface: A critical review, Energies 14 (1) (2020) 80.

[37] S. Mandre, M.P. Brenner, The mechanism of a splash on a dry solid surface, J. Fluid Mech. 690 (2012) 148–172.

[38] S. Lin, B. Zhao, S. Zou, J. Guo, Z. Wei, L. Chen, Impact of viscous droplets on different wettable surfaces: Impact phenomena, the maximum spreading factor, spreading time and post-impact oscillation, J. Colloid Interface Sci. 516 (2018) 86–97.

[39] M.-J. Thoraval, J. Schubert, S. Karpitschka, M. Chanana, F. Boyer, E. Sandoval-Naval, J.F. Dijksman, J.H. Snoeijer, D. Lohse, Nanoscopic interactions of colloidal particles can suppress millimetre drop splashing, Soft Matter 17 (20) (2021) 5116–5121.

[40] N. Kovalchuk, D. Johnson, V. Sobolev, N. Hilal, V. Starov, Interactions between nanoparticles in nanosuspension, Adv. Colloid Interface Sci. 272 (2019) 102020.

[41] S. Vafaei, T. Borca-Tasciuc, M. Podowski, A. Purkayastha, G. Ramanath, P. Ajayan, Effect of nanoparticles on sessile droplet contact angle, Nanotechnology 17 (10) (2006) 2523.

[42] A. Munshi, V. Singh, M. Kumar, J. Singh, Effect of nanoparticle size on sessile droplet contact angle, J. Appl. Phys. 103 (8) (2008).

[43] D.T. Wasan, A.D. Nikolov, Spreading of nanofluids on solids, Nature 423 (6936) (2003) 156–159.

[44] A.J. Harrison, D.S. Corti, S.P. Beaudoin, Capillary forces in nanoparticle adhesion: a review of AFM methods, Particul. Sci. Technol. 33 (5) (2015) 526–538.

[45] F. Babayekhorasani, D.E. Dunstan, R. Krishnamoorti, J.C. Conrad, Nanoparticle diffusion in crowded and confined media, Soft Matter 12 (40) (2016) 8407–8416.

[46] D. Mangal, J.C. Conrad, J.C. Palmer, Nanoparticle dispersion in porous media: Effects of hydrodynamic interactions and dimensionality, AIChE J. 67 (3) (2021) e17147.

[47] F. Babayekhorasani, D.E. Dunstan, R. Krishnamoorti, J.C. Conrad, Nanoparticle dispersion in disordered porous media with and without polymer additives, Soft Matter 12 (26) (2016) 5676–5683.

[48] H. Wu, D.K. Schwartz, Nanoparticle tracking to probe transport in porous media, Acc. Chem. Res. 53 (10) (2020) 2130–2139.

[49] M.J. Skaug, L. Wang, Y. Ding, D.K. Schwartz, Hindered nanoparticle diffusion and void accessibility in a three-dimensional porous medium, ACS Nano 9 (2) (2015) 2148–2156.

[50] R. Raccis, A. Nikoubashman, M. Retsch, U. Jonas, K. Koynov, H.-J. Butt, C.N. Likos, G. Fytas, Confined diffusion in periodic porous nanostructures, ACS Nano 5 (6) (2011) 4607–4616.

[51] I.C. Kim, S. Torquato, Diffusion of finite-sized Brownian particles in porous media, J. Chem. Phys. 96 (2) (1992) 1498–1503.

[52] H. Shen, L.J. Tauzin, R. Baiyasi, W. Wang, N. Moringo, B. Shuang, C.F. Landes, Single particle tracking: from theory to biophysical applications, Chem. Rev. 117 (11) (2017) 7331–7376.

[53] R. Metzler, J.-H. Jeon, A.G. Cherstvy, E. Barkai, Anomalous diffusion models and their properties: non-stationarity, non-ergodicity, and ageing at the centenary of single particle tracking, Phys. Chem. Chem. Phys. 16 (44) (2014) 24128–24164.

[54] D. Wang, H. Wu, L. Liu, J. Chen, D.K. Schwartz, Diffusive escape of a nanoparticle from a porous cavity, Phys. Rev. Lett. 123 (11) (2019) 118002.

[55] C. Scholz, F. Wirner, J.R. Gomez-Solano, C. Bechinger, Enhanced dispersion by elastic turbulence in porous media, Europhys. Lett. 107 (5) (2014) 54003.

[56] D.M. Walkama, N. Waisbord, J.S. Guasto, Disorder suppresses chaos in viscoelastic flows, Phys. Rev. Lett. 124 (16) (2020) 164501.

[57] C.C. Hopkins, S.J. Haward, A.Q. Shen, Tristability in viscoelastic flow past side-by-side microcylinders, Phys. Rev. Lett. 126 (5) (2021) 054501.

[58] D.W. Carlson, A.Q. Shen, S.J. Haward, Microtomographic particle image velocimetry measurements of viscoelastic instabilities in a three-dimensional microcontraction, J. Fluid Mech. 923 (2021).

[59] C. Fernandes, D. Semyonov, L.L. Ferrás, J.M. Nóbrega, Validation of the CFD-DPM solver DPMFoam in OpenFOAM® through analytical, numerical and experimental comparisons, Granul. Matter 20 (4) (2018) http://dx.doi.org/10.1007/s10035-018-0834-x.

[60] J.M. Ramirez, E.A. Thomann, E.C. Waymire, J. Chastanet, B.D. Wood, A note on the theoretical foundations of particle tracking methods in heterogeneous porous media, Water Resour. Res. 44 (1) (2008).

[61] D. Mangal, J.C. Palmer, J.C. Conrad, Nanoparticle dispersion in porous media: Effects of array geometry and flow orientation, Phys. Rev. E 104 (1) (2021) 015102.

[62] S. Aramideh, P.P. Vlachos, A.M. Ardekani, Nanoparticle dispersion in porous media in viscoelastic polymer solutions, J. Non-Newton. Fluid Mech. 268 (2019) 75–80.

[63] Y.T. Aksoy, L. Liu, M. Abboud, M.R. Vetrano, E. Koos, Role of nanoparticles in nanofluid droplet impact on solid surfaces, Langmuir 39 (1) (2022) 12–19.

[64] D. Zang, X. Wang, X. Geng, Y. Zhang, Y. Chen, Impact dynamics of droplets with silica nanoparticles and polymer additives, Soft Matter 9 (2) (2013) 394–400.

[65] F. Pimenta, M. Alves, 2016. See https://github.com/fppimenta/rheoTool for, Rheotool.

[66] H. Jasak, A. Jemcov, Z. Tukovic, et al., OpenFOAM: A C++ library for complex physics simulations, in: International Workshop on Coupled Methods in Numerical Dynamics, Vol. 1000, 2007, pp. 1–20.

[67] N. Phan-Thien, A nonlinear network viscoelastic model, J. Rheol. 22 (3) (1978) 259–283.

[68] L.L. Ferrás, J.M. Nóbrega, F.T. Pinho, Analytical solutions for channel flows of Phan-Thien–Tanner and Giesekus fluids under slip, J. Non-Newton. Fluid Mech. 171 (2012) 97–105.

[69] P.J. Oliveira, F.T. Pinho, Analytical solution for fully developed channel and pipe flow of Phan-Thien–Tanner fluids, J. Fluid Mech. 387 (1999) 271–280.

[70] C.M. Casciola, E. De Angelis, Energy transfer in turbulent polymer solutions, J. Fluid Mech. 581 (2007) 419–436.

[71] R. Guénette, M. Fortin, A new mixed finite element method for computing viscoelastic flows, J. Non-Newton. Fluid Mech. 60 (1) (1995) 27–52.

[72] C. Fernandes, M. Araujo, L. Ferrás, J.M. Nóbrega, Improved both sides diffusion (iBSD): A new and straightforward stabilization approach for viscoelastic fluid flows, J. Non-Newton. Fluid Mech. 249 (2017) 63–78.

[73] F. Pimenta, M. Alves, Stabilization of an open-source finite-volume solver for viscoelastic fluid flows, J. Non-Newton. Fluid Mech. 239 (2017) 85–104.

[74] J.L. Favero, A. Secchi, N.S.M. Cardozo, H. Jasak, Viscoelastic flow analysis using the software OpenFOAM and differential constitutive equations, J. Non-Newton. Fluid Mech. 165 (23–24) (2010) 1625–1636.

[75] R. Fattal, R. Kupferman, Constitutive laws for the matrix-logarithm of the conformation tensor, J. Non-Newton. Fluid Mech. 123 (2–3) (2004) 281–285.

[76] R. Fattal, R. Kupferman, Time-dependent simulation of viscoelastic flows at high weissenberg number using the log-conformation representation, J. Non-Newton. Fluid Mech. 126 (1) (2005) 23–37.

[77] F. Habla, M.W. Tan, J. Haßlberger, O. Hinrichsen, Numerical simulation of the viscoelastic flow in a three-dimensional lid-driven cavity using the log-conformation reformulation in OpenFOAM®, J. Non-Newton. Fluid Mech. 212 (2014) 47–62.

[78] F. Pimenta, M.A. Alves, A coupled finite-volume solver for numerical simulation of electrically-driven flows, Comput. & Fluids 193 (2019) 104279.

[79] D.A. Hoang, V. Van Steijn, L.M. Portela, M.T. Kreutzer, C.R. Kleijn, Benchmark numerical simulations of segmented two-phase flows in microchannels using the volume of fluid method, Comput. & Fluids 86 (2013) 28–36.

[80] L. Gamet, M. Scala, J. Roenby, H. Scheufler, J. Pierson, Validation of volume-of-fluid OpenFOAM® isoadvector solvers using single bubble benchmarks, Comput. & Fluids 213 (2020) 104722.

[81] S.S. Deshpande, L. Anumolu, M.F. Trujillo, Evaluating the performance of the two-phase flow solver interfoam, Comput. Sci. Discov. 5 (1) (2012) 014016.

[82] E. Berberović, N.P. Van H., S. Jakirlić, I.V. Roisman, C. Tropea, Drop impact onto a liquid layer of finite thickness: Dynamics of the cavity evolution, Phys. Rev. E 79 (3) (2009) 036306.

[83] J.U. Brackbill, D.B. Kothe, C. Zemach, A continuum method for modeling surface tension, J. Comput. Phys. 100 (2) (1992) 335–354.

[84] F. Greifzu, C. Kratzsch, T. Forgber, F. Lindner, R. Schwarze, Assessment of particle-tracking models for dispersed particle-laden flows implemented in OpenFOAM and ANSYS FLUENT, Eng. Appl. Comput. Fluid Mech. 10 (1) (2016) 30–43.

[85] C.T. Crowe, J.D. Schwarzkopf, M. Sommerfeld, Y. Tsuji, Multiphase Flows with Droplets and Particles, CRC Press, 2011, http://dx.doi.org/10.1201/b11103.

[86] P.A. Cundall, O.D. Strack, A discrete numerical model for granular assemblies, Geotechnique 29 (1) (1979) 47–65.

[87] C. O'Sullivan, Particulate Discrete Element Modelling: A Geomechanics Perspective, CRC Press, 2011.

[88] H.P. Zhu, Z.Y. Zhou, R. Yang, A. Yu, Discrete particle simulation of particulate systems: theoretical developments, Chem. Eng. Sci. 62 (13) (2007) 3378–3396.

[89] O. Mahian, L. Kolsi, M. Amani, P. Estellé, G. Ahmadi, C. Kleinstreuer, J.S. Marshall, M. Siavashi, R.A. Taylor, H. Niazmand, et al., Recent advances in modeling and simulation of nanofluid flows-Part I: Fundamentals and theory, Phys. Rep. 790 (2019) 1–48.
[90] A. Li, G. Ahmadi, Dispersion and deposition of spherical particles from point sources in a turbulent channel flow, Aerosol Sci. Technol. 16 (4) (1992) 209–226.
[91] J. Mewis, N.J. Wagner, Colloidal suspension rheology, Cambridge University Press, 2012.
[92] Y. Tsuji, T. Tanaka, T. Ishida, Lagrangian numerical simulation of plug flow of cohesionless particles in a horizontal pipe, Powder Technol. 71 (3) (1992) 239–250.
[93] C.J. Greenshields, OpenFOAM Programmer's Guide, OpenFOAM Foundation Ltd, 2015.
[94] A.H. Slim, R. Poling-Skutvik, J.C. Conrad, Local confinement controls diffusive nanoparticle dynamics in semidilute polyelectrolyte solutions, Langmuir 36 (31) (2020) 9153–9159.
[95] J.D. Jacob, R. Krishnamoorti, J.C. Conrad, Particle dispersion in porous media: Differentiating effects of geometry and fluid rheology, Phys. Rev. E 96 (2) (2017) 022610.
[96] L. Campagnolo, M. Nikolić, J. Perchoux, Y.L. Lim, K. Bertling, K. Loubiere, L. Prat, A.D. Rakić, T. Bosch, Flow profile measurement in microchannel using the optical feedback interferometry sensing technique, Microfluid. Nanofluid. 14 (1–2) (2013) 113–119.
[97] L. Zheng, A.W. Schmid, J.C. Lambropoulos, Surface effects on Young's modulus and hardness of fused silica by nanoindentation study, J. Mater. Sci. 42 (2007) 191–198.
[98] H.K. Huh, S. Jung, K.W. Seo, S.J. Lee, Role of polymer concentration and molecular weight on the rebounding behaviors of polymer solution droplet impacting on hydrophobic surfaces, Microfluid. Nanofluid. 18 (2015) 1221–1232.
[99] Y.T. Aksoy, P. Eneren, E. Koos, M.R. Vetrano, Spreading of a droplet impacting on a smooth flat surface: How liquid viscosity influences the maximum spreading time and spreading ratio, Phys. Fluids 34 (4) (2022).
[100] N. Phan-Thien, H.-S. Dou, Viscoelastic flow past a cylinder: drag coefficient, Comput. Methods Appl. Mech. Engrg. 180 (3–4) (1999) 243–266.